




# The Cellular Characterization of SARS-CoV-2 Spike Protein in Virus-Infected Cells Using the Receptor Binding Domain Binding Specific Human Monoclonal Antibodies

Conrad En-Zuo Chan,<sup>a,b</sup> Ching-Ging Ng,<sup>a</sup> Angeline Pei-Chew Lim,<sup>a</sup> Shirley Lay-Kheng Seah,<sup>a</sup> De-Hoe Chye,<sup>a</sup> Steven Ka-Khuen Wong,<sup>a</sup> Jie-Hui Lim,<sup>a</sup> Vanessa Zi-Yun Lim,<sup>c</sup> Soak-Kuan Lai,<sup>c</sup> Pui-San Wong,<sup>a</sup> Kok-Mun Leong,<sup>a</sup> Yi-Chun Liu,<sup>a</sup> Richard J. Sugrue,<sup>c</sup>  Boon-Huan Tan<sup>a,c,d</sup>

<sup>a</sup>Biological Defence Programme, DSO National Laboratories, Singapore, Republic of Singapore

<sup>b</sup>Infectious Disease Laboratory, National Centre for Infectious Diseases, Singapore, Republic of Singapore

<sup>c</sup>School of Biological Sciences, Nanyang Technological University, Singapore, Republic of Singapore

<sup>d</sup>Infection and Immunity, LKC School of Medicine, Nanyang Technological University, Singapore, Republic of Singapore

**ABSTRACT** A human monoclonal antibody panel (PD4, PD5, PD7, SC23, and SC29) was isolated from the B cells of convalescent patients and used to examine the S protein in SARS-CoV-2-infected cells. While all five antibodies bound conformational-specific epitopes within SARS-CoV-2 spike (S) protein, only PD5, PD7, and SC23 were able to bind to the receptor binding domain (RBD). Immunofluorescence microscopy was used to examine the S protein RBD in cells infected with the Singapore isolates SARS-CoV-2/0334 and SARS-CoV-2/1302. The RBD-binders exhibited a distinct cytoplasmic staining pattern that was primarily localized within the Golgi complex and was distinct from the diffuse cytoplasmic staining pattern exhibited by the non-RBD-binders (PD4 and SC29). These data indicated that the S protein adopted a conformation in the Golgi complex that enabled the RBD recognition by the RBD-binders. The RBD-binders also recognized the uncleaved S protein, indicating that S protein cleavage was not required for RBD recognition. Electron microscopy indicated high levels of cell-associated virus particles, and multiple cycle virus infection using RBD-binder staining provided evidence for direct cell-to-cell transmission for both isolates. Although similar levels of RBD-binder staining were demonstrated for each isolate, SARS-CoV-2/1302 exhibited slower rates of cell-to-cell transmission. These data suggest that a conformational change in the S protein occurs during its transit through the Golgi complex that enables RBD recognition by the RBD-binders and suggests that these antibodies can be used to monitor S protein RBD formation during the early stages of infection.

**IMPORTANCE** The SARS-CoV-2 spike (S) protein receptor binding domain (RBD) mediates the attachment of SARS-CoV-2 to the host cell. This interaction plays an essential role in initiating virus infection, and the S protein RBD is therefore a focus of therapeutic and vaccine interventions. However, new virus variants have emerged with altered biological properties in the RBD that can potentially negate these interventions. Therefore, an improved understanding of the biological properties of the RBD in virus-infected cells may offer future therapeutic strategies to mitigate SARS-CoV-2 infection. We used physiologically relevant antibodies that were isolated from the B cells of convalescent COVID-19 patients to monitor the RBD in cells infected with SARS-CoV-2 clinical isolates. These immunological reagents specifically recognize the correctly folded RBD and were used to monitor the appearance of the RBD in SARS-CoV-2-infected cells and identified the site where the RBD first appears.

**KEYWORDS** SARS-CoV-2, S protein, receptor binding domain (RBD), human monoclonal antibodies, convalescent patient serum, furin, cell-to-cell transmission

**Editor** Mark T. Heise, University of North Carolina at Chapel Hill

**Copyright** © 2022 American Society for Microbiology. All Rights Reserved.

Address correspondence to Boon-Huan Tan, tboonhua@dso.org.sg, Conrad En-Zuo Chan, Conrad\_EZ\_CHAN@ncid.sg, or Richard J. Sugrue, rjsugrue@ntu.edu.sg.

The authors declare no conflict of interest.

**Received** 24 March 2022

**Accepted** 13 May 2022

**Published** 21 June 2022

Coronavirus disease 2019 (COVID-19) is a new respiratory-borne infectious disease caused by severe acute respiratory syndrome coronavirus 2 (SARS-CoV-2) (1, 2). Since its first formal identification in Wuhan City, Hubei Province, China, in 2019, SARS-CoV-2 has been responsible for approximately 255 million infections and 5.1 million deaths worldwide (<https://covid19.who.int/>, accessed 19 November 2021). The SARS-CoV-2 virus belongs to the *Coronaviridae* family, which includes both established coronaviruses that usually cause mild to moderate respiratory disease in humans (e.g., the human coronavirus 229E), and newer emerging viruses that are associated with high mortality rates in humans (e.g., SARS-CoV-1) (3–5). SARS-CoV-2, like other coronaviruses, contains a positive-sense, nonsegmented, and single-stranded RNA genome (vRNA) and contains between 10 to 14 open reading frames (ORF), which encode various virus proteins in the following order: 5' untranslated region (UTR), replicase (ORF1a/1b), spike (S), envelope (E), membrane (M), nucleocapsid (N), 3' UTR, and poly A tail (6). The mature SARS-CoV-2 particle is surrounded by a lipid envelope that is derived from the host cell, and into which the M, E, and S proteins are inserted. Since the first published sequence of SARS-CoV-2 was isolated in Wuhan (WIV04) (7), new sequence variants of SARS-CoV-2 have been identified (e.g., Alpha, Beta, Gamma, and Delta variants) that exhibit variations in the virus genome sequences that change the biological properties of the virus (<https://www.who.int/en/activities/tracking-SARS-CoV-2-variants/>, accessed 20 November 2021). It is postulated that these changes may also lead to increased virus transmission and lead to altered immunogenicity in humans (8–10). Therefore, an improved understanding of the biology of new and existing circulating SARS-CoV-2 variants is required to better understand the risks that these variants pose.

The S protein mediates the entry of the virus into the host cell, and it thus plays an essential role in initiating the virus infection. The S protein exists as a homotrimer and protrudes from the virus envelope as an array of club-like projections. It is a dominant feature on the surface of virus particle, and this topology is a defining feature in coronavirus identification using diagnostic electron microscopy. The virus envelope surrounds internal virus structures, such as the virus nucleocapsid, which is formed by the association between the vRNA and the N protein. The entry of the SARS-CoV-2 genome into susceptible cells occurs by fusion of the virus envelope and cell membrane, and the S protein mediates both the cell attachment (via the cell receptor), and the fusion of the virus and cell membranes. The S protein is initially synthesized as a single polypeptide chain (S<sub>0</sub>), and it is subsequently cleaved into the S1 and S2 subunits at two cleavage sites. The S1 domain contains the receptor binding domain (RBD), which mediates binding of the virus to the target cell via angiotensin-converting enzyme 2 (ACE2) host cell receptor. The S2 domain is anchored to the virus envelope by a transmembrane domain, and it contains the fusion peptide and heptad repeat regions that mediate the process of membrane fusion. Unlike the SARS-CoV-1 S protein, the cleavage site of the S protein of SARS-CoV-2 contains the sequence RRAR at the S1/S2 site, which is recognized by the ubiquitous cellular protease furin (reviewed in reference 11). A second cleavage site within the S2 domain (the S2' site) is required during the early stages of virus cell entry; however, cleavage at the S1/S2 site is required for S2' cleavage (12). Although cleavage at the S2' site is mediated by transmembrane protease serine 2 (TMPRSS2), TMPRSS2 is not expressed in Vero E6 cells (13) and it is proposed that the S2' cleavage site can also be processed by other cellular proteases in these cells (14).

The S protein has also become a focus in the development of antiviral drug strategies using small-molecule inhibitors and passive immunization using human monoclonal antibodies (hMAbs) (15). Given the importance of the S protein RBD during virus cell attachment, these immunological reagents often target the RBD to prevent the initial stages of SARS-CoV-2 entry into host cells. The isolation of hMAbs from the B cells of convalescent serum can be used in passive immunization for the timely treatment and prevention of SARS-CoV-2 infection, and the discovery of hMAbs from COVID-19 convalescent patients has shown therapeutic potential (16–19). A number of these

have been granted emergency authorization and have progressed through clinical trials for use as antibody therapeutics (20, 21). Although the emphasis has been on the development of reagents that can block the RBD, the potential use of non-RBD-binders with virus neutralizing activity as part of a cocktail of antibody therapeutics is also expected to overcome problems associated with the emergence of new virus variants (17). The most important practical criterion for these immunological reagents is that they neutralize virus infection by, e.g., blocking attachment of the virus to the host cell. However, it is also expected that these reagents could also provide other useful information about the biology of the S protein of existing and newly emerged SARS-CoV-2 variants. The individual monoclonal antibodies could also potentially form part of a wider polyclonal immune response during SARS-CoV-2 infection, and characterizing the individual monoclonal antibodies could provide useful information about how these antibody responses interact with the virus. We have previously described a panel of S protein hMAbs that were isolated using the B cells of convalescent COVID-19 patients in Singapore (19). These antibodies were originally isolated for evaluation as potential therapeutic interventions in SARS-CoV-2-infected patients. In the current study we have used RBD-specific antibodies in this hMAb panel to examine the cellular properties of the S protein RBD in virus-infected African green monkey kidney epithelial cells (Vero E6 cells). Our experimental approach is aimed to complement the ongoing high-resolution structural studies of the S protein undertaken by other groups and the interaction of the RBD with neutralizing antibodies (22, 23). Our current analysis was performed using SARS-CoV-2 clinical isolates that were isolated during the early phase of the pandemic in Singapore. These immunological reagents also allowed us to perform a comparison of the biological properties of these SARS-CoV-2 clinical isolates in infected cells.

## RESULTS AND DISCUSSION

**The Singapore SARS-CoV-2 isolates and the hMAb panel used in this study.** In this study, we used three SARS-CoV-2 viruses that were isolated during the early phase of the COVID-19 pandemic in Singapore, which are referred to as SARS-CoV-2/1302, SARS-CoV-2/0563, and SARS-CoV-2/0334. Since the characterization of the S protein hMAbs was the major focus of this study, the complete S protein sequence for each isolate used in our analysis was determined. Each virus isolate was passaged three times in Vero E6 cells, and the genetic material extracted from each passage was PCR-amplified with specific primers for the S gene and sequenced using Sanger's sequencing. The sequences from overlapping amplicons were assembled and analyzed. The data revealed that the nucleotide and amino acid sequences of the S protein from the three Singapore isolates had a high level of sequence homology to the S sequence of the SARS-CoV-2/WIV04 isolate (GenBank accession no. [MN996528](#)) that was reported when the COVID 19 pneumonia first originated in Wuhan in China (7). In the first passage the S protein sequence of each virus isolate was identical to the S protein sequence of the SARS-CoV-2/WIV04 isolate (see Fig. S1 in the supplemental material). However, the subsequent passages of the virus during virus stock amplification showed some specific changes in the primary amino acid sequences of the S protein. The S protein sequences of SARS-CoV-2/0334 and SARS-CoV-2/0563 comprised 1,269 amino acids and were 100% identical. Each had a five-amino acid deletion in the S protein sequence at <sup>675</sup>QTQTN<sub>679</sub> that was just upstream of the polybasic furin cleavage site (Fig S1). Although the <sup>675</sup>QTQTN<sub>679</sub> deletion was not observed in the S protein sequence of SARS-CoV-2/1302, the S protein sequence of SARS-CoV-2/1302 had a single amino acid change, R682W, in the furin cleavage site. This created <sup>682</sup>WRARS<sub>686</sub> rather than the complete furin consensus sequence <sup>682</sup>RRARS<sub>686</sub>, which is found in the S protein sequences of SARS-CoV-2/WIV04, SARS-CoV-2/0563, and SARS-CoV-2/0334. Virus variants, also known as quasi-species, containing mutations in the region of the S1/S2 protein proteolytic cleavage site have been reported to be present in SARS-CoV-2-infected patients (24), and these can be selected during passaging of the virus in

tissue culture. The basis for this virus selection and the selective advantage that these sequence changes impart to the virus isolate in tissue culture are currently unclear. Apart from the sequence differences indicated above, the remaining S protein sequence of each of the Singapore isolates was 100% identical to the S protein sequence of SARS-CoV-2/WIV04. In particular, the sequence of the S protein RBD was 100% identical in SARS-CoV-2/WIV04 and all three of the Singapore SARS-CoV-2 isolates. Since the S protein sequences of the SARS-CoV-2/0563 and SARS-CoV-2/0334 isolates were identical, all subsequent work on characterizing immune-reactivity of the hMAb panel was performed mainly using the SARS-CoV-2/1302 and SARS-CoV-2/0334 isolates.

In this study, we selected PD4, PD5, PD7, SC23, and SC29 from the original antibody panel for further characterization using a cellular virology approach, but recognition of S protein by each antibody in the panel was confirmed by using the purified SARS-CoV-2 S protein ectodomain in an enzyme-linked immunosorbent assay (ELISA) (Fig. 1A). In a similar analysis using a sequence that corresponded to the S protein RBD, only PD5, PD7, and SC23 showed RBD binding (RBD-binders) (Fig. 1Bi). It is presumed that the epitopes recognized by the RBD-binders are formed by different parts of the RBD once it had folded into the correct conformation. Although comparable binding affinities to the complete S protein were noted for all hMAbs, the SC23 showed reduced binding affinity for the RBD compared with PD5 or PD7 (Fig. 1Bii and C). This indicated that SC23 may recognize a distinct sequence in the RBD and that one or more sequences located outside the RBD may facilitate its binding to the RBD. No RBD binding was detected by PD4 and SC29, suggesting that the SC29 and PD4 epitope recognition sequences were outside the RBD region.

The differential recognition of the RBD was further supported by examining the ability of the hMAb panel to block SARS-CoV-2 binding to Vero E6 cells using a virus neutralization assay. Only PD5, PD7, and SC23 exhibited virus neutralizing activity, while PD4 and SC29 failed to inhibit infection (Fig. 1D). These data indicated that inhibition of SARS-CoV-2 infection correlated with RBD recognition, and it is presumed that binding of the antibodies to the RBD would create a steric hindrance that would interfere with the virus attachment to the cell receptor.

We failed to detect binding of these antibodies to the S protein using Western blotting (Fig. 1E). The folding pattern in the RBD is expected to be lost during the sample processing process in the Western blot analysis, and the inability of these antibodies to bind to the S protein in Western blot analysis provided evidence that the RBD-binders bind to conformational-specific epitopes on the correctly folded S protein. Although we have not mapped the binding domains of PD4 and SC29, we examined their binding activities using an ELISA-based antibody-binding competition assay (Fig. 1F). This assay indicated that the binding of PD4 and SC29 antibodies to the S protein was mutually exclusive, suggesting that PD4 and SC29 bind to similar locations on the S protein. Prior binding of either the PD5, PD7, or SC23 antibody to the S protein did not interfere with PD4 or SC29 binding, which was consistent with PD4 and SC29 being non-RBD-binders. Binding of the PD5, PD7, and SC23 antibodies to the S protein in the same antibody-binding competition assay were also mutually exclusive, indicating binding to similar locations on the S protein and consistent with their RBD-binding properties. There was a general correlation between the RBD recognition and the complementarity-determining region (CDRs) sequences of the individual antibodies in the hMAb panel. There was a high degree of similarity between the sequence of the CDRs of PD5 and PD7 and to a lesser extent with SC23 (Fig. 1G), which correlated with the different RBD-binding activity of SC23. The PD4 and SC29 showed high levels of sequence similarity in CDR1 and CDR2 in the heavy chain and were distinct from the CDRs in the RBD-binders.

**Distribution of the S protein RBD in SARS-CoV-2-infected Vero E6 cells.** The recognition of S protein by each antibody in the hMAb panel was further confirmed by examining their immunoreactivity in SARS-CoV-2-infected Vero E6 cells (Fig. 2A). Vero

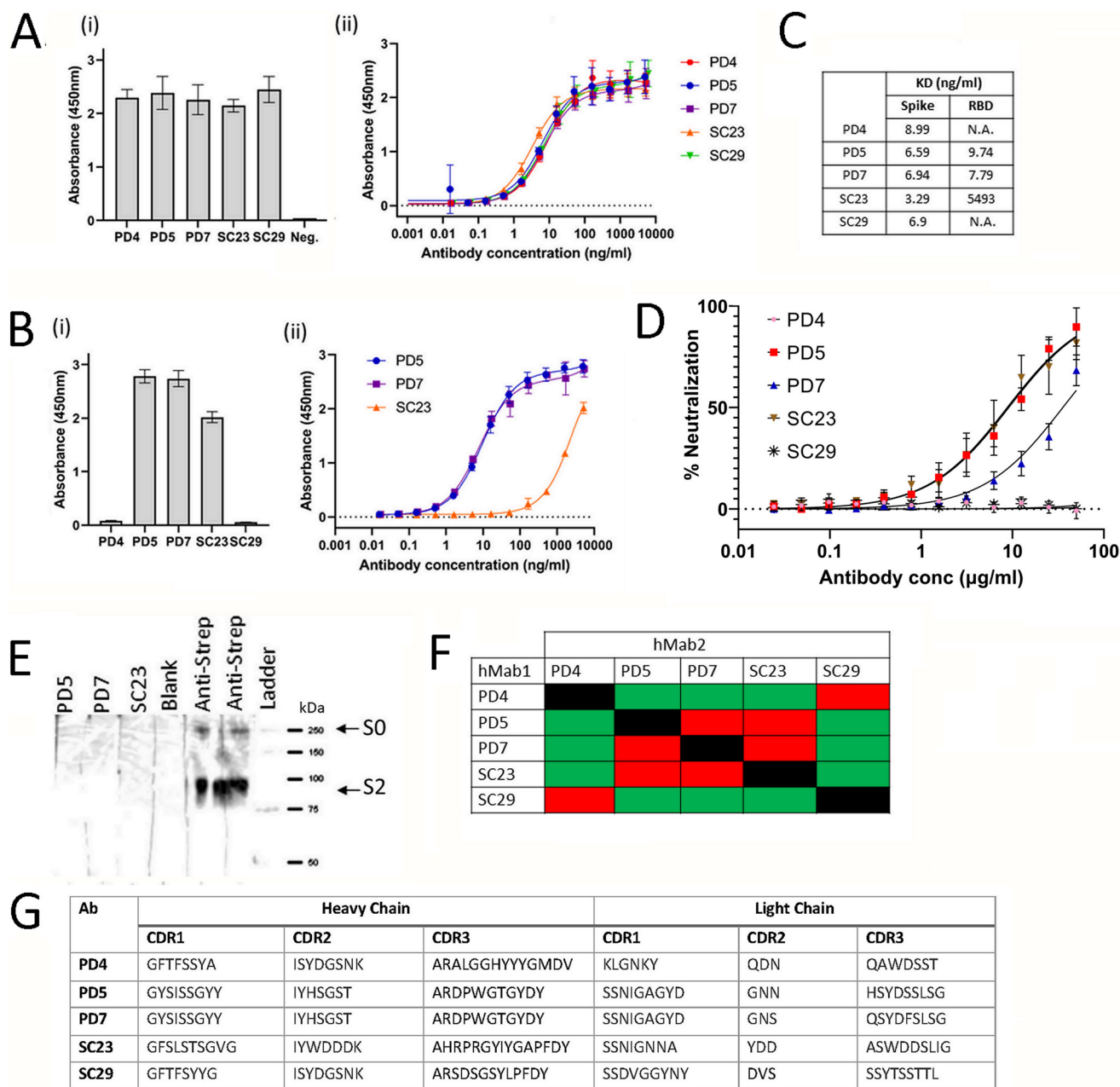


**FIG 1** Specificity of anti-SARS-CoV-2 human monoclonal antibodies (hMAbs) used in this study. The binding affinities to the spike (S) protein and neutralization activity with SARS-CoV-2 virus was determined for each hMAB in the panel, PD4, PD5, PD7, SC23, and SC29. (A) (i) Binding affinity of the hMAB panel against the extracellular domain of the S protein by enzyme-linked immunosorbent assay (ELISA). (ii) Binding affinity of the hMAB panel to the S protein as a function of antibody concentration from 0.001 to 10,000 ng/mL. (B) (i) Binding of the hMAB panel to the receptor binding domain (RBD) of the S protein as measured by ELISA; (ii) binding of PD5, PD7, and SC23 to the RBD of S protein as a function of antibody concentration from 0.001 to 10,000 ng/mL. (C) The binding affinities to the extracellular domain and the RBD of S protein was determined for each member of the hMAB panel and measured in the dissociation constant (KD in ng/mL) (NA, not applicable). (D) Neutralization activity of the hMAB panel with 100 TCID<sub>50</sub> of infectious SARS-CoV-2 and measured as a function of antibody concentration (Antibody conc) from 0.01 to 100 μg/mL. Neutralization efficacy is represented as a percentage relative to uninfected and virus-only controls. (E) The recombinant SARS-CoV-2 S-Strep protein was transferred to a polyvinylidene difluoride (PVDF) membrane by Western blotting, and the PVDF membrane was cut into strips and incubated with PD5, PD7, or SC23, followed by secondary antibodies conjugated with horse radish peroxidase (HRP). The lane labeled “Blank” refers to a blank lane, and the lanes labeled “Anti-Strep” refers to incubation with anti-Strep conjugated to HRP as the loading control (positive S protein control). The protein species corresponding in size to the uncleaved S0 and S2 are highlighted. “Ladder” represents protein standards from 37 to 250 kDa. (F) In the ELISA-based antibody binding competition assay each of the hMAbs (PD4, PD5, PD7, SC23, SC29) was coated in a well (hMAB1), and the recombinant S protein was bound to the coated antibody. Different hMAbs (hMAB2) were then added to the bound S protein, and binding was assessed by ELISA. Red, binding of the specific hMAB1 inhibits the specific hMAB2 antibody binding; green, binding of the specific hMAB1 has no effect on the specific hMAB2 antibody binding. (G) The sequences of the complementarity-determining regions (CDRs) for members of the antibody panel. The CDR1-3 sequences are shown for the heavy and light chains for each corresponding antibody.

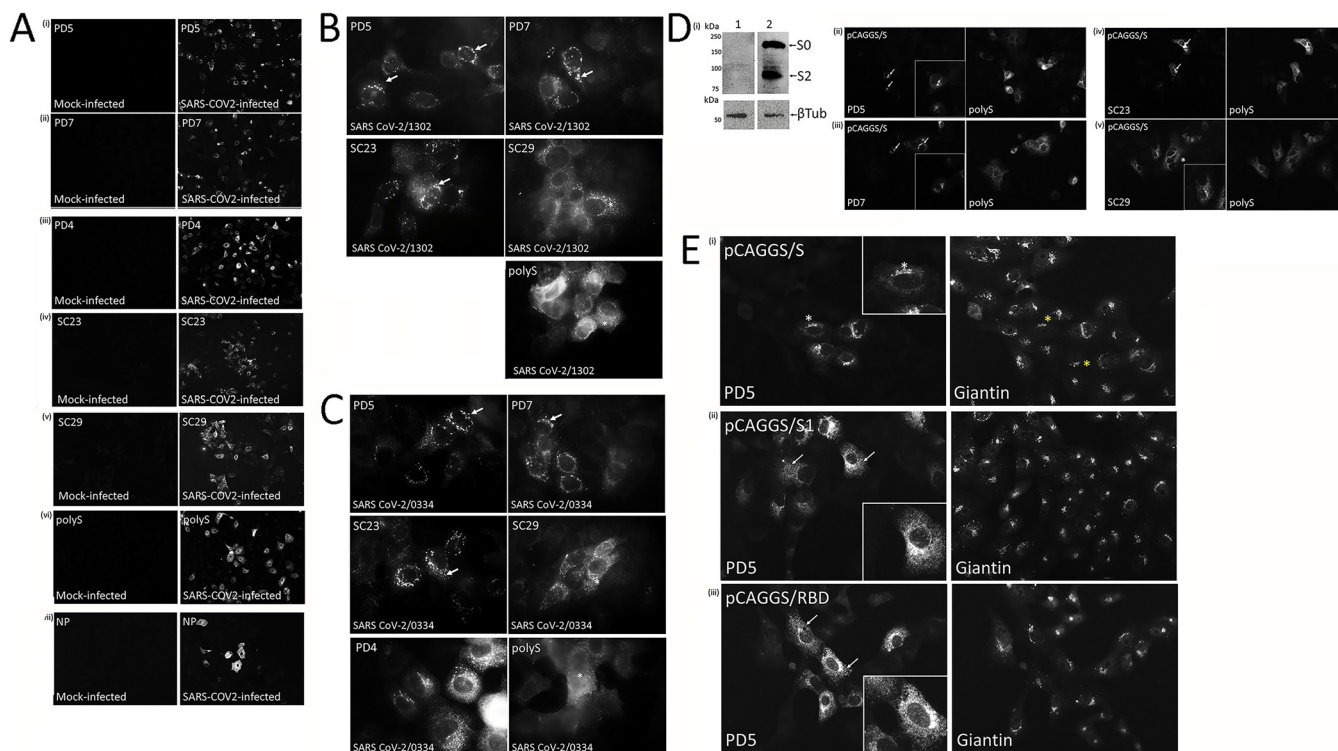


**FIG 2** Immune reactivity of the anti-SARS-CoV-2 human monoclonal antibodies in virus-infected Vero E6 cells. (A) At 18 h postinfection (hpi), mock-infected and SARS-CoV-2/0334-infected cells were stained using (i) PD5, (ii) PD7, (iii) PD4, (iv) SC23, (v) SC29, (vi) polyS, and (vii) anti-NP and imaged using immunofluorescence (IF) microscopy (objective  $\times 40$  magnification). (B and C) Vero E6 cells were infected with (B) SARS-CoV-2/1302 and (C) SARS-CoV-2/0334, and at 18 hpi the cells were costained using PD5, PD7, PD4, SC23, SC29, and polyS as indicated. The stained cells were imaged using IF microscopy (objective  $\times 100$  magnification; oil immersion). The prominent punctate cytoplasmic staining pattern (white arrow) is highlighted. (D) (i) Cells were (1) mock-transfected and transfected with (2) pCAGGS/S, and the lysates were immunoblotted with polyS. Protein species corresponding in size to the uncleaved (S0) and S2 domain of the S protein are indicated. Tubulin is the loading control. Cells were transfected with pCAGGS/S and costained with polyS and (ii) PD5, (iii) PD7, (iv) SC23, and (v) SC29 as indicated. The stained cells were imaged by IF microscopy (objective  $\times 40$  magnification). The diffuse cytoplasmic S protein staining (\*) and punctate cytoplasmic staining (white arrows) are indicated. (E) Cells were transfected with (i) pCAGGS/S, (ii) pCAGGS/S1, and (iii) pCAGGS/RBD as indicated and costained with PD5 and anti-giantin. The costained cells were imaged by IF microscopy (objective  $\times 40$  magnification). The inset is an enlarged image of a representative cell showing the specific PD5 staining in each case.

E6 cells were either mock-infected or infected with SARS-CoV-2/0334, and at 18 h post-infection (hpi) the cells were stained using either PD5, PD7, PD4, SC23, or SC29 (Fig. 2A). Imaging using immunofluorescence (IF) microscopy showed that fluorescence staining using either antibody was only detected in the virus-infected cells, indicating S protein recognition by the hMAb panel. Virus infection was confirmed by using the commercially available S protein polyclonal antibody (polyS) that recognizes the S2 domain and the N protein antibody (anti-NP).

Cells infected with either SARS-CoV-2/1302 (Fig. 2B) or SARS-CoV-2/0334 (Fig. 2C) were stained with PD5, PD7, PD4, SC23, SC29, and polyS and examined in greater detail using IF microscopy. In SARS-CoV-2-infected cells stained with PD5, PD7, and SC23, a similar prominent punctate cytoplasmic staining pattern was apparent, while cells stained with either PD4 or SC29 exhibited a more distinct cytoplasmic staining pattern. These staining patterns were defined as being representative if they were observed in greater than 94% of the cells in the field of view using IF microscopy (e.g., at  $\times 20$  magnification) and in several replicate experiments (i.e., more than 4 individual experiments). The diffuse PD4 or SC29 staining pattern was similar in appearance to the staining pattern exhibited by polyS-stained virus-infected cells. The imaging data therefore indicated that the hMAb panel could be divided into two groups based on their staining pattern in virus-infected cells, a prominent localized punctate staining pattern (PD5, PD7, and SC23) or a more broadly diffuse cytoplasmic staining pattern (PD4 and SC29), and these antibody-staining patterns correlated with RBD-recognition. These data suggested that the RBD-binders (e.g., PD5) may recognize a distinct

population of the S protein which allows recognition of the RBD. Since the polyS is a polyclonal S protein antibody, it would be expected to detect different forms of the S protein in virus-infected cells, albeit by recognizing the S2 domain.

In noninfected Vero E6 cells expressing the recombinant S protein, cell lysates were prepared and examined by immunoblotting with polyS (Fig. 2Di). S protein species corresponding in size to the uncleaved S protein (S<sub>0</sub>) and to the S2 domain were detected, which confirmed that the recombinant S protein was correctly processed in the transfected cells. The recognition of the S protein in the immunoblotting assay by polyS also suggested that recognition of the S protein by this antibody involved one or more of the linear epitopes rather than conformational-specific epitopes in the hMAb panel. Cells expressing the recombinant S protein were costained with polyS and either PD5, PD7, SC23, or SC29 and examined using IF microscopy (Fig. 2Dii to v), and staining of the transfected cells with either antibody confirmed the S protein recognition. We also compared the PD5 staining in cells expressing the full-length recombinant S protein with those expressing either only the S1 domain or the RBD (Fig. 2E). A more widespread PD5 staining pattern was observed in cells expressing the S1 domain and the RBD compared with the cells expressing the full-length S protein sequence. This confirmed that the RBD can form into its distinct structure independently of the S2 domain and indicated that the PD5 can recognize the RBD at other locations in cells expressing the S protein. This further supports the suggestion that in SARS-CoV-2-infected cells PD5 may recognize a distinct population of the S protein in which the RBD is accessible to antibody binding.

The IF microscopy analysis described above allowed several antibody-stained cells to be imaged in the same field of view, allowing representative antibody staining patterns to be determined. In contrast, confocal microscopy allows the detailed imaging of the antibody staining in individual representative cells. Since the respective antibody staining patterns were similar for both SARS-CoV-2 isolates, we used confocal microscopy to examine the staining pattern for each antibody in SARS-CoV-2/0334-infected Vero E6 cells. At 18 hpi the cells were costained with polyS and either PD5, PD7, PD4, SC23, or SC29, and a series of images was recorded in the Z-plane from individual representative costained cells. Single images were extracted at an optical plane from the Z-series that allowed the cytoplasmic staining patterns of the different antibodies to be compared (Fig. 3A). The polyS antibody exhibited a diffuse cytoplasmic staining pattern, but a small degree of colocalization within the distinct prominent punctate staining pattern exhibited by PD5, PD7, and SC23 was noted. This punctate staining pattern was also exhibited in PD4- and SC29-stained virus-infected cells; however, these antibodies also exhibited additional prominent diffuse SC29 and PD4 staining patterns. These different antibody staining patterns suggested that the PD5, PD7, and SC23 only recognize a specific subpopulation of the total S protein in which the protein conformation renders the RBD accessible to antibody binding. The recognition of the S protein by PD4 and SC29 was not dependent on RBD recognition, and the additional diffuse antibody staining pattern suggested that they recognize other forms of the S protein. A similar imaging analysis of transfected cells expressing the recombinant S protein and costained with polyS and PD5 and SC29 was also performed. This showed the distinct antibody-specific staining patterns that were similar to that observed in SARS-CoV-2-infected cells (Fig. 3B), in which the PD5 staining exhibited a general localized staining pattern compared with the more widespread staining pattern of SC29. This is consistent with similar processing of the recombinant S protein and the S protein expressed in virus-infected cells and indicated that the different S protein antibody staining patterns that we observed were not dependent on virus infection.

The C terminus of the S protein contains an endoplasmic reticulum (ER) retrieval signal which facilitates the accumulation of the S protein close to the site of coronavirus particle assembly (25). The process of coronavirus assembly involves the ER-Golgi intermediate compartment (ERGIC) and Golgi complex (6). The S protein undergoes a series of important posttranslational modifications that are mediated by cellular activities associated with the Golgi complex (e.g., glycosylation, furin cleavage), and in virus-infected cells we examined

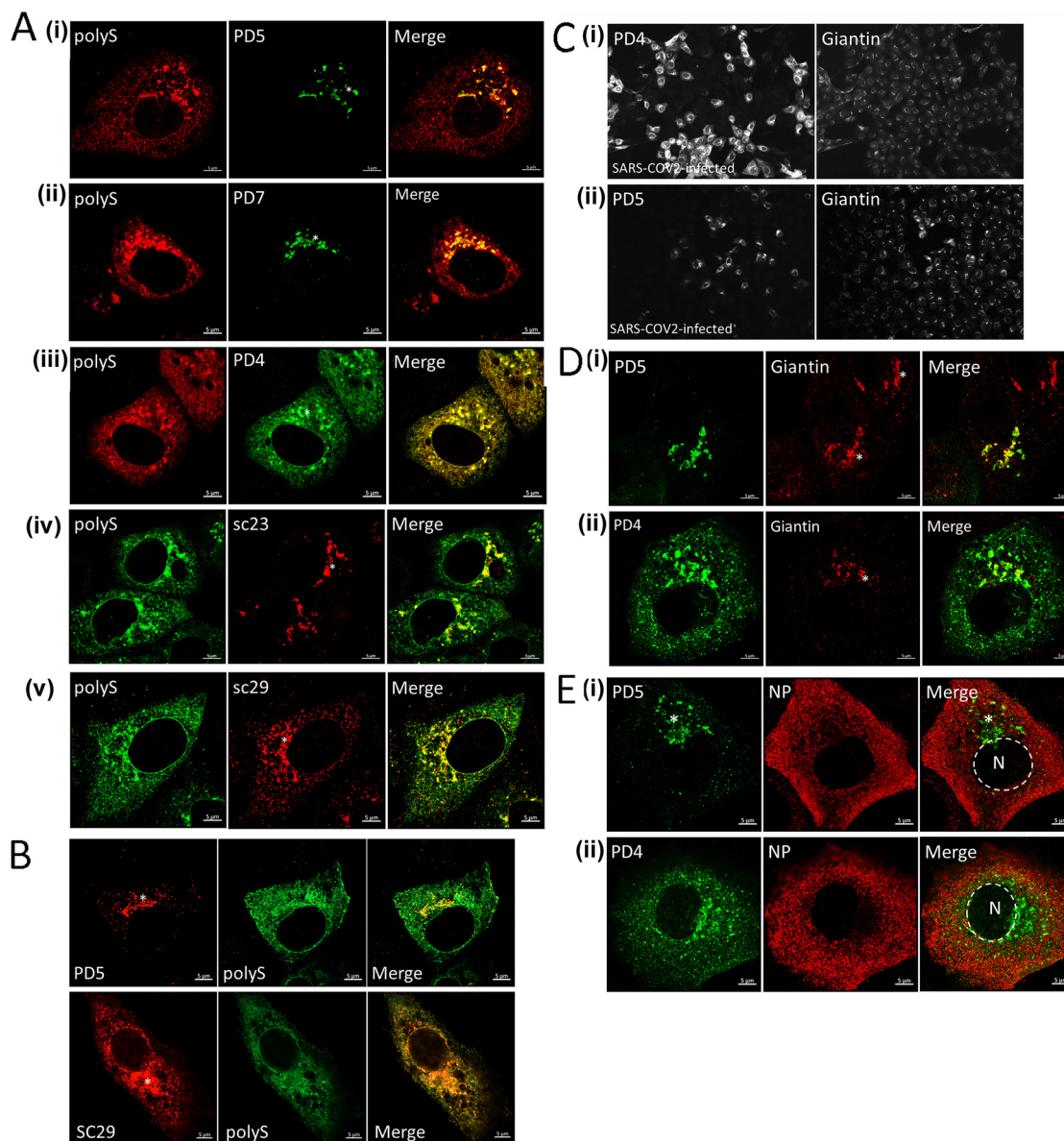


**FIG 3** Distribution of the S protein RBD and Golgi complex in virus-infected Vero E6 cells. (A) At 18 h postinfection SARS-CoV-2/0334-infected cells were costained using anti-polyS and either (i) PD5, (ii) PD7, (iii) PD4, (iv) SC23, or (v) SC29 and imaged using confocal microscopy. The individual channel and merged images are shown. The prominent punctate cytoplasmic staining pattern (\*) is highlighted. (B) Vero E6 cells expressing recombinant S protein were costained with anti-polyS and either PD5 or SC29 and imaged using confocal microscopy. The individual channel and merged images are shown. (C) SARS-CoV-2/0334-infected cells were costained using (i) PD4 and antigiantin and (ii) PD5 and anti-giantin and imaged using immunofluorescence microscopy (objective  $\times 20$  magnification). (D) SARS-CoV-2/0334-infected cells were costained using (i) PD5 and antigiantin and (ii) PD4 and antigiantin and imaged using confocal microscopy. The giantin staining pattern indicating the Golgi complex (\*) is highlighted. (E) SARS-CoV-2/0334-infected cells were costained using (i) PD5 and anti-NP and (ii) PD4 and anti-NP and imaged using confocal microscopy. The punctate PD5 staining pattern (\*) and area of the nucleus (N and delineated by the white broken line) are indicated. In all confocal microscope images the individual channel images and merged images are shown.

the staining patterns of the RBD-binders in the context of the Golgi complex. The PD5, PD7, and SC23 exhibited similar staining patterns within infected cells, and we concluded that imaging of PD5 staining could be used as a representative of this antibody group (RBD-binders). Mock- and SARS-CoV-2/0334-infected Vero E6 cells were costained with PD5 or PD4 and antigiantin (a Golgi complex marker) and imaged using IF microscopy. Although some costaining between PD4 and antigiantin was noted, the overall diffuse PD4 staining pattern contrasted with the localized antigiantin staining pattern (Fig. 3Ci). Similar PD5 and antigiantin staining patterns in virus-infected cells were noted (Fig. 3Cii),



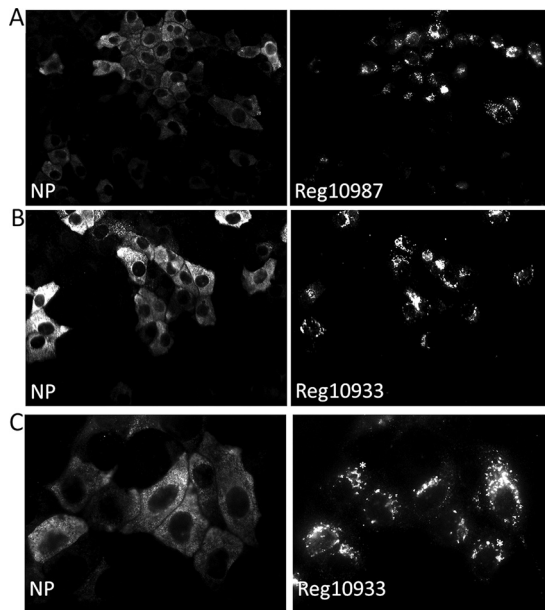


**FIG 4** Vero E6 cells infected with SARS-CoV-2 and stained with monoclonal antibodies whose receptor binding domain (RBD) recognition sites have been defined. (A to C) SARS-CoV-2/0334-infected Vero E6 cells were costained with either (A) REGEN-10987 (Reg10987) or (B and C) REGEN-10933 (Reg10933) and anti-NP (recognizes the SARS-CoV-2 N protein). In all cases images were recorded using immunofluorescence microscopy. Panels A and B, objective  $\times 20$  magnification; panel C, objective  $\times 100$  magnification.

indicating that PD5 staining was largely localized to elements of the Golgi complex. A more detailed analysis of the antibody staining patterns was performed using confocal microscopy on PD5 and PD4 cells containing anti-giantin (Fig. 3D). This revealed a high level of colocalization between the punctate PD5 staining pattern and the Golgi complex in infected cells (Fig. 3Dii and iii) and (Fig S3F) and confirmed that the punctate PD5 staining pattern was mainly restricted to the Golgi complex. The PD4 staining exhibited the diffuse antibody staining described above, which only partially localized with the anti-giantin staining at the Golgi complex (Fig. 3Di). The infected cells were also costained with either PD5 or PD4 and anti-NP and imaged using confocal microscopy (Fig. 3E). The anti-NP labeling gives rise to a prominent cytoplasmic staining pattern that allowed delineation of the infected cells, and the absence of nuclei staining with this antibody enables the position of the nucleus to be visualized. This staining combination therefore allows the respective PD5 and PD4 staining pattern to be visualized in the context of the whole cell.

We also examined the staining pattern of REGEN-10933 and REGEN-10987, whose binding sites in the S protein RBD have been accurately defined using structural biology (26, 27). SARS-CoV-2/0334-infected cells were costained with either REGEN-10987 or REGEN-10933 and anti-NP (Fig. 4). The anti-NP gave rise to a broadly cytoplasmic staining pattern that delineated the body of the cell, which contrasted with the localized and punctate staining pattern exhibited by REGEN-10933 and REGEN-10987. The REGEN-10933 and REGEN-10987 antibodies also showed staining patterns that were similar to the staining patterns exhibited by the RBD-binders in virus-infected cells.

These data suggested that RBD recognition by PD5 occurs as the S protein is trafficked through the Golgi complex. The reason for the apparent accumulation of the S protein at the Golgi complex during its transport through the secretory pathway is currently unclear, but it may be related to the extensive glycosylation of the S protein (28). Although virus assembly is proposed to occur close to the Golgi complex, a similar PD5 staining pattern was also observed in transfected cells expressing the recombinant S protein, suggesting that this Golgi localization may not be directly caused by virus-induced changes in the secretory pathway.

The imaging data described above demonstrated the specificity of the hMAb panel

with regard to the S protein recognition in virus-infected Vero E6 cells and demonstrated specific antibody staining patterns that correlated with RBD-binding. Furthermore, these data also indicated that the deleted sequence  $_{675}\text{QTQTN}_{679}$  in SARS-CoV-2/0334 and the R682W change in SARS-CoV-2/1302 (Fig. S1) did not prevent recognition by either of the antibodies examined. We have failed to detect PD5 costaining with antibodies against early compartments of the secretory pathway, e.g., the ER compartment (R. J. Sugrue, unpublished observations), suggesting that PD5 staining is only detected in the later compartments of the secretory pathway. The more widespread cytoplasmic staining of the non-RBD-binders and polyS is presumably due to recognition of the S protein at other cellular locations (in addition to the Golgi complex). These data therefore suggest that while the non-RBD-binders and polyS recognize the total S protein expressed in virus-infected cells, the RBD-binders recognize only a subset of the total S protein where the RBD is antibody accessible. Although the Golgi compartment may be modified in SARS-CoV-2-infected cells to facilitate virus replication, the staining pattern of the RBD-binders (exemplified by PD5) was mainly associated with the Golgi complex. Since PD5 recognizes conformational-specific epitopes within the RBD of the S protein, these data suggest that a conformational change in the S protein may occur that leads to the correctly folded RBD at the Golgi complex that enabled PD5 recognition.

**The hMAbs recognize the RBD displayed on virus particles on the surface of SARS-CoV-2/1302- and SARS-CoV-2/0334-infected Vero E6 cells.** We used imaging to examine the surface expression of the S protein on infected Vero E6 cells stained with each of the antibodies in the hMAb panel. Vero E6 cells were mock infected (Fig. 5A) and infected with either SARS-CoV-2/0334 (Fig. 5Bi) or SARS-CoV-2/1302 (Fig. 5Bii), and at 18 hpi the nonpermeabilized cells were costained using PD5 and polyS and imaged using IF microscopy. A similar diffuse surface-staining pattern was noted on cells infected with either virus isolate. A similar surface-staining pattern was also observed on nonpermeabilized cells infected with SARS-CoV-2/0334 and costained with polyS and either PD7, SC23, or SC29 (Fig. 5C). The surface staining with the PD5, PD7, and SC23 antibodies indicated that the RBD was displayed on the surface of infected cells. Although SC29 did not recognize the RBD and did not exhibit virus neutralization activity, surface staining on SC29-stained nonpermeabilized cells indicated that the SC29 epitopes were also surface-displayed.

The surface-staining patterns were confirmed by comparing the PD5-staining patterns of nonpermeabilized cells and permeabilized SARS-CoV-2/0334-infected cells. Wheat germ agglutinin conjugated to Alexa 488 (WGA-488) is an established cellular probe that stains cellular membranes and cells, and were costained with PD5 and WGA-488 and imaged by IF microscopy (Fig. 5D). As expected, the PD5 staining pattern observed on nonpermeabilized cells (Fig. 5Di) was clearly distinct from the PD5 punctate cytoplasmic staining pattern exhibited on permeabilized cells (Fig. 5Dii). The nonpermeabilized SARS-CoV-2/0334-infected cells were costained using PD5 and polyS and examined in greater detail using confocal microscopy. A series of images was recorded in the Z-plane from individual representative costained cells, which allowed surface staining at the cell top (Fig. 5Ei) and at the cell periphery to be imaged (Fig. 5Eii). Both antibodies exhibited a similar surface-staining pattern on the costained cells, which appeared as small spots and filaments, and was distinct from the cytoplasmic PD5 and polyS staining patterns in permeabilized cells described above. The level of colocalization of these antibodies was examined using the Pearson's and Mander's correlation coefficients (Fig. 5F), which indicated a high level of colocalization between the two antibodies. A high level of costaining between both antibodies would be expected since both antibodies would be expected to recognize the same population of the S protein on the surface of infected cells. The surface-staining pattern exhibited by both antibodies was more apparent in a 3-D reconstruction of the nonpermeabilized costained infected cell (Fig. 5Gi and ii), where the filamentous costaining pattern was clearly distinguished from the spotted antibody staining pattern.

The surface topology of Vero E6 cells infected with SARS-CoV-2 isolates was further examined using scanning electron microscopy (SEM) to better understand the

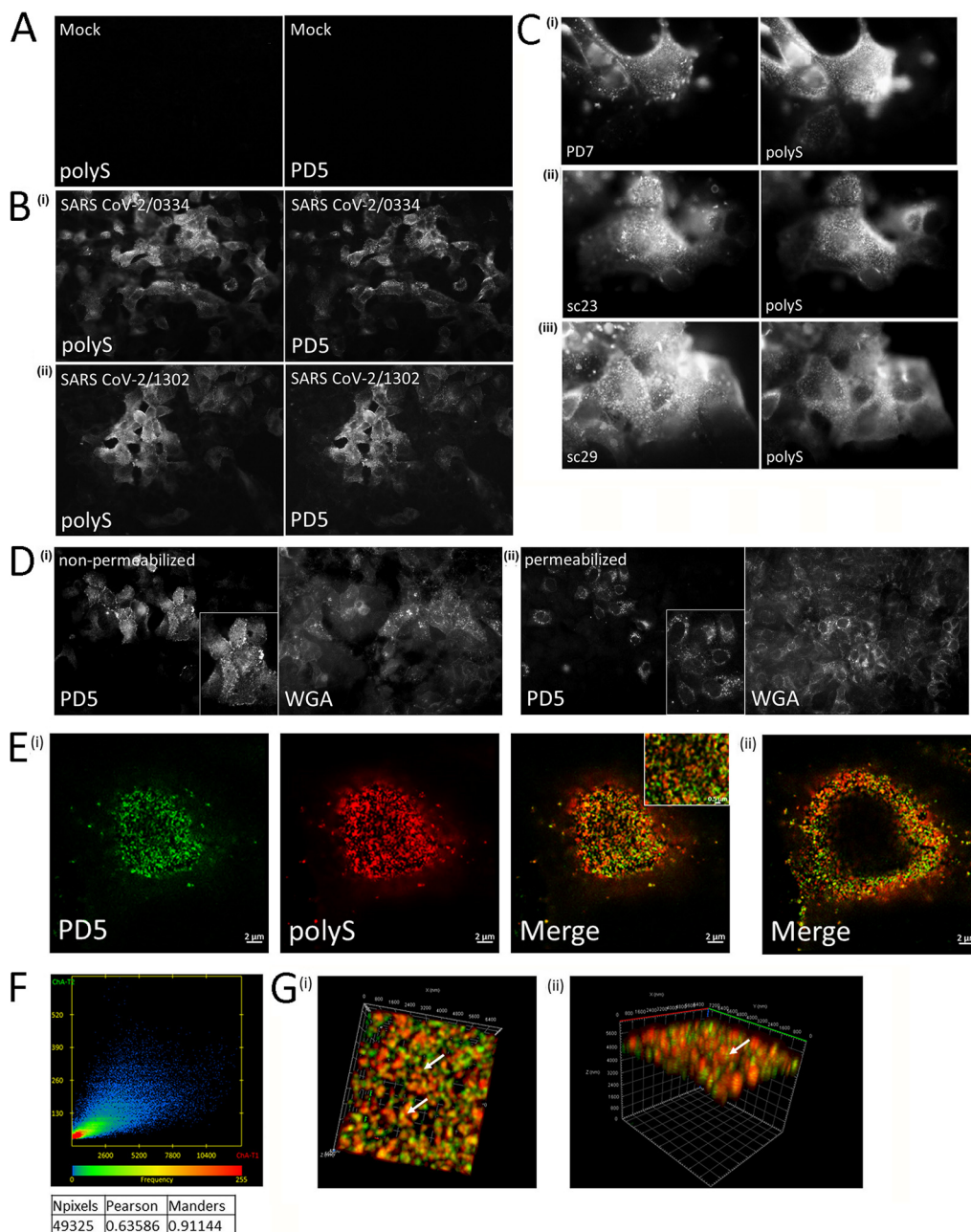


**FIG 5** Surface staining of SARS-CoV-2-infected Vero E6 cells. (A and B) Vero E6 cells were (A) mock-infected and (B) infected with (i) SARS-CoV-2/0334 or (ii) SARS-CoV-2/1302. At 18 h postinfection (hpi) the nonpermeabilized cells were costained using polyS and PD5. The stained cells were imaged using immunofluorescence (IF) microscopy (objective  $\times 40$  magnification). (C) Nonpermeabilized SARS-CoV-2/0334-infected cells were costained with polyS and either (i) PD7, (ii) SC23, or (iii) SC29. The stained cells were imaged using IF microscopy (objective  $\times 100$  magnification; oil immersion). (D) At 18 hpi SARS-CoV-2/0334-infected cells were (i) nonpermeabilized and (ii) permeabilized, and the cells were costained using PD5 and wheat germ agglutinin conjugated to Alexa 488 (WGA). The stained cells were imaged using IF microscopy (objective  $\times 40$  magnification). In both (i) and (ii) the inset is an enlarged imaged showing the PD5 staining pattern in each condition. (E) Vero E6 cells were infected with SARS-CoV-2/0334, and at 18 hpi the nonpermeabilized cells were costained using PD5 and polyS. The costained cells were imaged using confocal microscopy, and a series of images from the stained cell was obtained in the Z-plane. Individual optical slices from the (i) cell top and (ii) at the cell periphery are shown. The individual channels and merged images are shown, and an inset in (i) highlights the staining patterns at higher magnification. (F) The scatterplot and the values for the Pearson's and Mander's coefficients are shown from the 49,325 pixels sampled in the costained image. (G) The 3-dimensional reconstruction of the Z-stack series of images is shown. The reconstructed image is viewed from (i) above and (ii) at the side of the costained cell. The PD5 and polyS filamentous costained pattern on the cell surface is highlighted (white arrows).

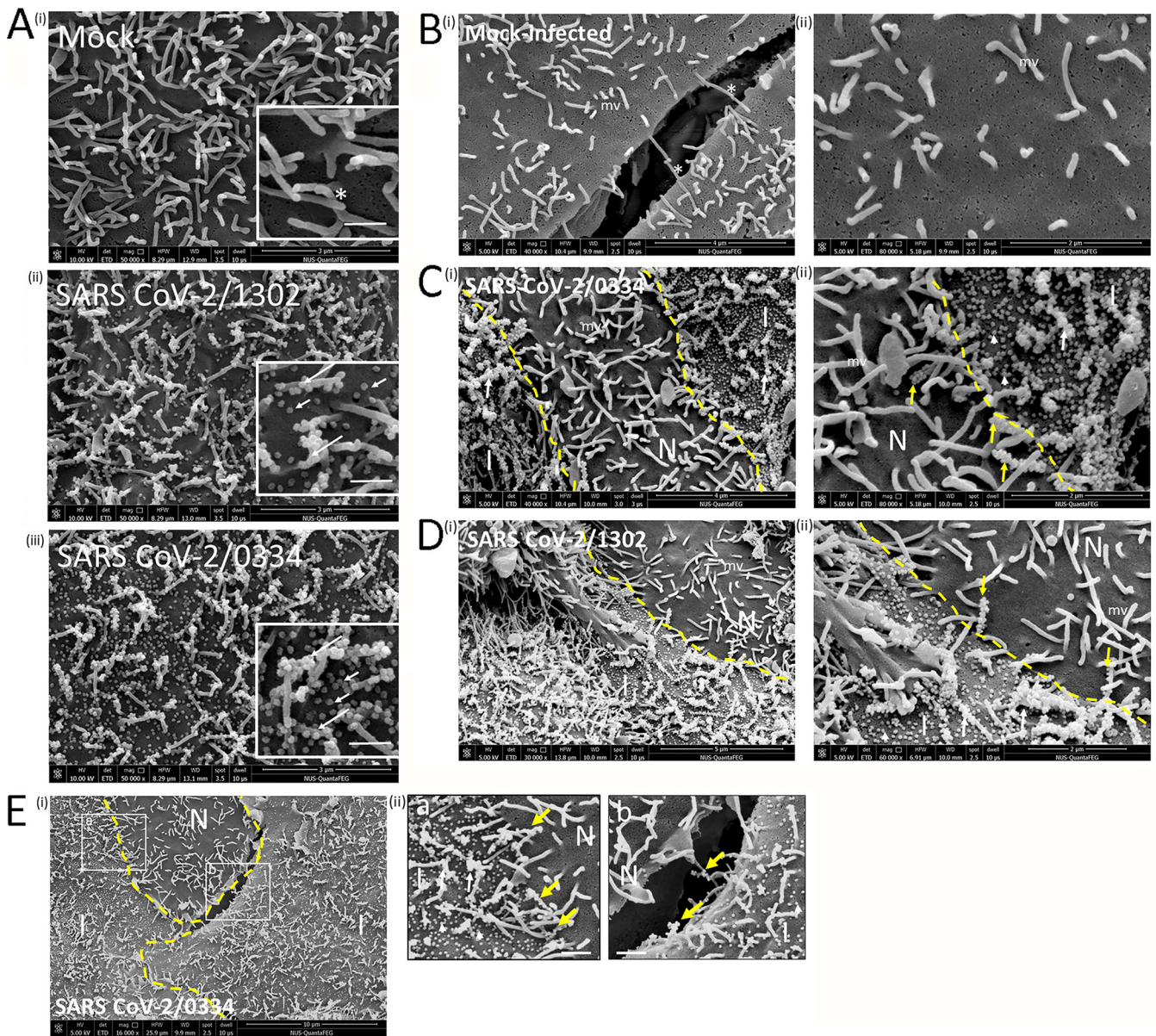


**FIG 6** Distribution of SARS-CoV-2 virus particles on the surface of infected Vero E6 cells. (A) (i) Mock-infected cells and cells infected with (ii) SARS-CoV-2/1302 and (iii) SARS-CoV-2/0334 at 18 h postinfection (hpi) were imaged using scanning electron microscopy ( $\times 50,000$  magnification). In each case the associated inset is an enlargement (white bar = 500 nm). The individual virus particles on the cell surface (short arrows) and clusters of virus particles associated with cell microvilli (long arrows) are highlighted. The microvilli on the surface of mock-infected cells are also highlighted (\*). (B to E) (B) Mock-infected Vero E6 cells and cells infected with (C) SARS-CoV-2/0334, (D) SARS-CoV-2/1302, and (E) SARS-CoV-2/0334 were imaged using scanning electron microscopy at 18 hpi. In each case microvilli (mv), infected (I) and noninfected (N) cells, the borders between different cells (broken yellow line), individual virus particles (white arrowhead), virus particles on microvilli (white arrows), virus particles on microvilli spanning different cells (yellow arrow), and microvilli spanning different cells in mock-infected cell monolayer (\*) are highlighted with (B and C)  $\times 40,000$  magnification, (Bii, and Dii)  $\times 80,000$  magnification, (Di)  $\times 30,000$  magnification, (Cii)  $\times 60,000$  magnification, and (Ei)  $\times 16,000$  magnification. (Eii) Panels a and b are enlarged images from the area demarcated by the open white boxes in panel i. The white bars in panel Eii represent 1  $\mu\text{m}$ .

relevance of the different surface-staining patterns detected in the confocal microscope analysis described above. Cells were either mock-infected or infected with SARS-CoV-2/1302 and SARS-CoV-2/0334 isolates and at 18 hpi were imaged using SEM (Fig. 6A). Numerous surface projections were observed on the surface of the mock-infected cells, which was consistent with the presence of microvilli (Fig. 6Ai), and these structures were also present on the surface of cells infected with SARS-CoV-2/1302 (Fig. 6Aii) and SARS-CoV-2/0334 (Fig. 6Aiii). The SARS-CoV-2 particles are approximately 80 to 100 nm in diameter (29), and the numerous spherical particles

of similar uniform dimensions that were detected on the surface of the virus-infected cells were consistent with the presence of individual SARS-CoV-2 particles. Approximately 70% of these virus particles were also associated with the microvilli projections, and we estimated that up to 10 virus particles could be detected on many microvilli. Microvilli extending from individual cells to neighboring cells in the monolayer was a common occurrence on mock-infected cells (Fig. 6B), indicating that under normal conditions these surface structures can make direct physical connections to neighboring cells. In this context, cells infected with either isolate showed virus particles on these microvilli extending from visibly infected cells to neighboring noninfected cells in the cell monolayer was noted (Fig. 6B to E), suggesting that these preexisting surface projections may serve as conduits to facilitate localized cell-to-cell transmission of SARS-CoV-2 in the cell monolayers. This is consistent with the recent interpretations of SARS-CoV-2 transmission in infected Vero cell monolayers (30, 31). Although the significance of the association of SARS-CoV-2 particles with these cellular projections is uncertain, this explains the apparent filamentous PD5 and polyS costaining pattern observed in the confocal microscopic analysis.

A comparison of the imaging data by light microscopy and SEM provided evidence that the surface staining correlated with the appearance of SARS-CoV-2 particles on the surface of infected cells. This indicated that surface-PD5 staining could be used to detect virus particles on the surface of SARS-CoV-2-infected cells. The surface staining of SC29 also provided evidence that the nonneutralizing antibodies can also bind to the virus particles on the surface of the infected cells. Although the RBD-binders recognize the S protein at the Golgi complex, the surface PD5 staining suggested that the antibodies also recognized the S protein in post-Golgi transport compartments in which the virus particles are transported to the surface of infected cells.

**Establishing the kinetics of cell-to-cell spread for SARS-CoV-2/1302 and SARS-CoV-2/0334 in the Vero E6 cell monolayers.** The SEM analysis indicated that large numbers of SARS-CoV-2 particles were present on the surface of infected Vero E6 cells, suggesting that a high level of virus infectivity remained cell-associated at this time of infection. We estimated that on average more than 200 virus particles/cell were detected on SARS-CoV-2/0334-infected cells, which is in the same order of magnitude as the estimated burst size for other coronaviruses (32). In addition, we consistently noted lower numbers of virus particles on SARS-CoV-2/1302-infected cells compared than on SARS-CoV-2/0334 virus-infected Vero E6 cells. Since the cells were exposed to similar levels of each virus isolate [multiplicity of infection (MOI) of 0.1] and examined at the same time of infection, these differences suggested a slower rate of appearance of virus particles (i.e., virus particle assembly) in SARS-CoV-2/1302-infected Vero E6 cells, and this was examined further. Vero E6 cell monolayers were infected with SARS-CoV-2/1302 or SARS-CoV-2/0334 using MOIs of 0.001 (Fig. 7A), 0.01 (Fig. 7B), and 0.1 (Fig. 7C), and at 18 hpi the cell monolayers were costained using PD5 and polyS and imaged by IF microscopy. At all MOI values examined, the two virus isolates exhibited an antibody staining pattern that was largely composed of clusters of stained cells. This was consistent with the localized cell-to-cell virus transmission, in which the progeny virus particles produced in the initial virus-infected cell infected the immediate surrounding cells in the monolayer. If high levels of infectious SARS-CoV-2 were shed into the tissue culture medium covering the infected cells, a more sporadic antibody labeling pattern would be expected that consisted of higher numbers of individual stained cells randomly distributed in the monolayer. It was noticeable that the cells infected with SARS-CoV-2/1302 consistently exhibited smaller infected cell clusters ( $10 \pm 1.5$  cells per cluster; MOI = 0.01) than the cells infected with the SARS-CoV-2/0334 isolate ( $25 \pm 2.1$  cells per cluster; MOI = 0.01) (Fig. 7D), which suggested reduced cell-to-cell transmission exhibited by SARS-CoV-2/1302. The clustered staining pattern consistent with localized cell-to-cell transmission of these virus isolates was further supported by examining the relative level of virus infectivity that was cell-free (tissue culture supernatant) and cell-associated (cell mass), and in cells infected with either isolate, the cell-associated virus infectivity accounted for a higher

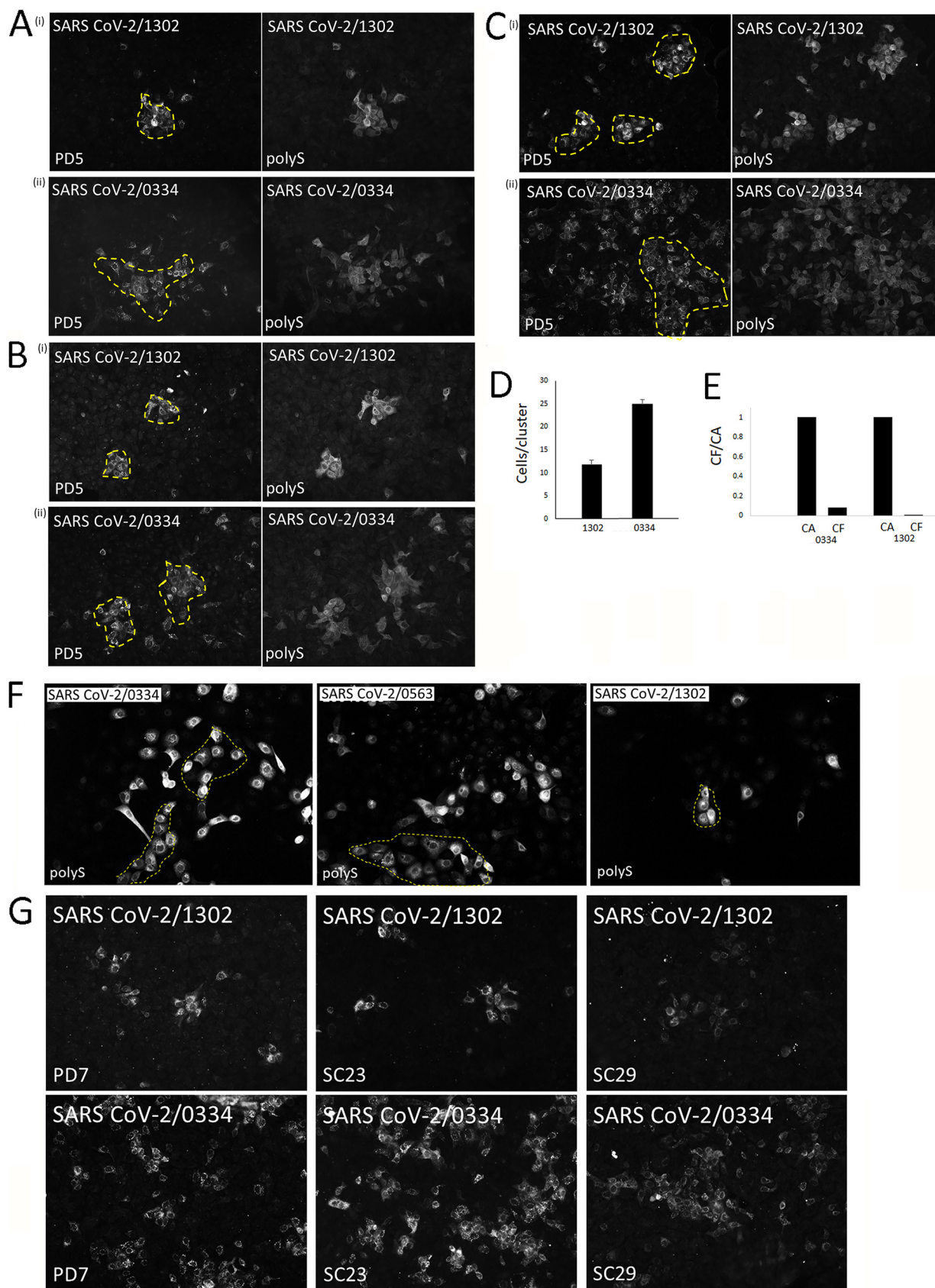


**FIG 7** Comparison of Vero E6 cells infected with SARS-CoV-2/1302 and SARS-CoV-2/0334 at different multiplicities of infection (MOI). (A to C) Vero E6 cells were infected with (i) SARS-CoV-2/1302 and (ii) SARS-CoV-2/0334 using an MOI of (A) 0.001, (B) 0.01, and (C) 0.1, and at 18 h (Continued on next page)

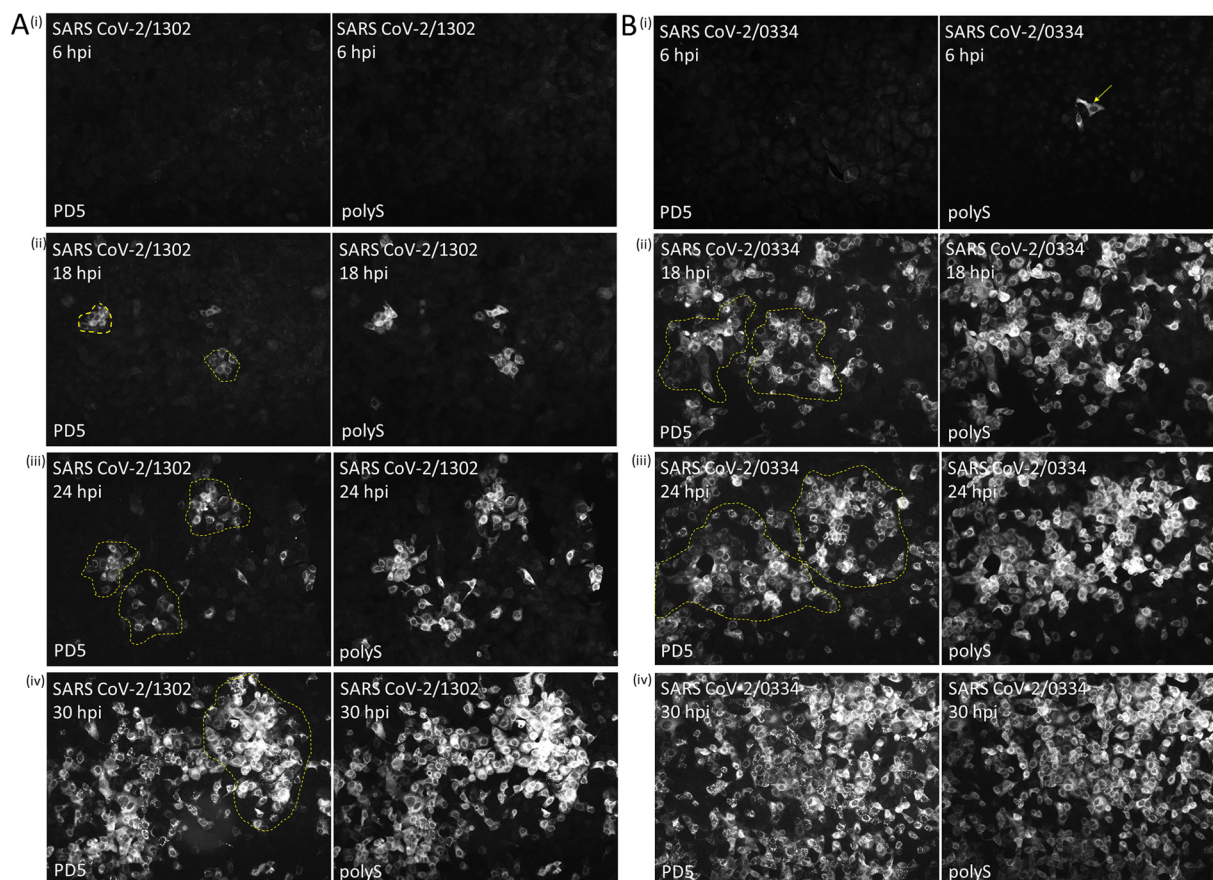


**FIG 8** Temporal appearance of PD5 and anti-polyS staining on Vero E6 cells infected with SARS-CoV-2/1302 and SARS-CoV-2/0334. (A and B) Vero E6 cells were infected with (A) SARS-CoV-2/1302 virus and (B) SARS-CoV-2/0334 using an multiplicity of infection (MOI) of 0.01, and at (i) 6 h postinfection (hpi), (ii) 18 hpi, (iii) 24 hpi, and (iv) 30 hpi the cells were costained with PD5 and polyS. The stained cells were imaged using immunofluorescence microscopy (objective  $\times 20$  magnification). A sporadic infected cell at 6 hpi is highlighted (white arrow), and in both panels A and B clusters of infected cells are highlighted (broken yellow line).

proportion of the total infectivity (approximately 90% of the total recovered infectivity) (Fig. 7E). In this context cells infected with SARS-CoV-2/0563 and stained using polyS also showed infected cell clusters that were of a similar size to those in SARS-CoV-2/0334-infected cells (Fig. 7F). This clustered antibody staining was also observed on PD7-, SC23-, and SC29-stained SARS-CoV-2/1302- and SARS-CoV-2/0334-infected cells (Fig. 7G), indicating that the clustered staining pattern was not antibody-specific (i.e., due to PD5 and polyS staining). This interpretation of localized virus transmission of these SARS-CoV-2 isolates was consistent with recent observations of SARS-CoV-2 transmission reported by other laboratories (30).

These data provide evidence for localized cell-to-cell transmission in the cell monolayer and suggest that SARS-CoV-2/0334 exhibited a faster rate of transmission than SARS-CoV-2/1302. The kinetics of virus spread in the Vero cell monolayer was determined in Vero E6 cells infected with SARS-CoV-2/1302 (Fig. 8A) or SARS-CoV-2/0334

**FIG 7** Legend (Continued)

postinfection (hpi) the cells were costained using PD5 and polyS, and imaged using immunofluorescence (IF) microscopy (objective  $\times 20$  magnification). In each condition the representative infected cell clusters are highlighted (broken yellow line). (D) The average numbers of infected cells per infected cell cluster in cells infected with SARS-CoV-2/1302 (1302) and SARS-CoV-2/0334 (0334) using an MOI of 0.01 are shown. (E) The relative levels of cell-associated (CA) and cell-free (CF) virus infectivity recovered from cells infected with SARS-CoV-2/0334 (0334) and SARS-CoV-2/1302 (1302) using an MOI of 0.01. In this analysis the results are presented as a fraction of the CA infectivity (which is set to a value of 1.0). (F) Cells were infected with SARS-CoV-2/0334, SARS-CoV-2/0563, and SARS-CoV-2/1302 as indicated using an MOI of 0.01. At 18 hpi the cells were stained with polyS. In all cases images were recorded using IF microscopy (objective  $\times 20$  magnification). (G and C) Cells were infected with (G) SARS-CoV-2/1302 and (C) SARS-CoV-2/0334 using an MOI of 0.01, and at 18 hpi the cells were stained with PD7, SC23, and SC29 as indicated.

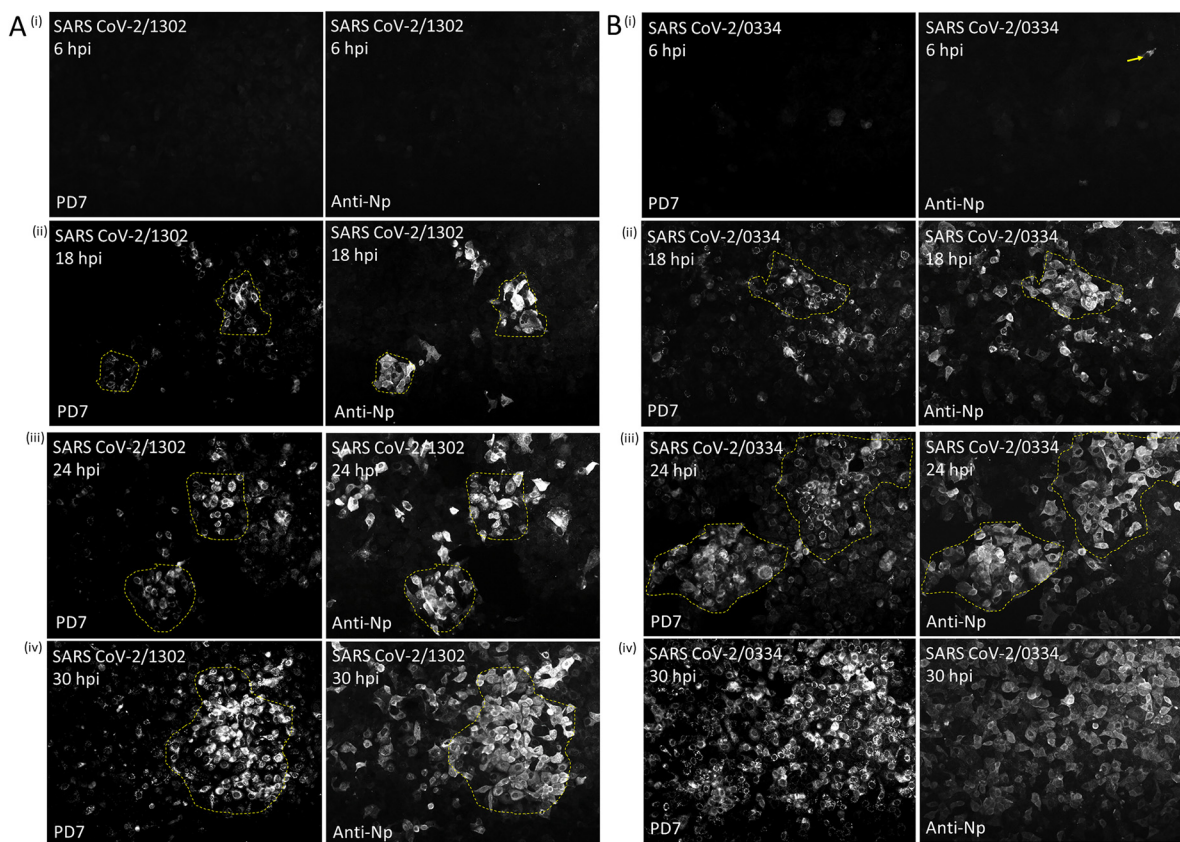


**FIG 9** Temporal appearance of PD7 and anti-N protein staining on Vero E6 cells infected with SARS-CoV-2/1302 and SARS-CoV-2/0334. (A and B) Cells were infected with (A) SARS-CoV-2/1302 and (B) SARS-CoV-2/0334 using an multiplicity of Infection (MOI) of 0.01, and at (i) 6 h postinfection (hpi), (ii) 18 hpi, (iii) 24 hpi, and (iv) 30 hpi the cells were costained with PD7 and anti-N protein (NP). The stained cells were imaged using immunofluorescence microscopy (objective  $\times 20$ ). In both panels A and B, clusters of infected cells are highlighted (broken yellow line).

(Fig. 8B) using an MOI of 0.01. At between 6 and 30 hpi the cells were costained with PD5 and polyS and examined by IF microscopy. At 6 hpi we failed to detect significant levels of virus infectivity, suggesting that this is at a time prior to significant levels of progeny virus production. At 18 hpi the appearance of infected cell clusters could be readily detected in cell monolayer infected with either isolate, which became progressively larger at 24 and 30 hpi. These rates of virus spread in the cell monolayers are consistent with previous reports that have examined the replication kinetics of SARS-CoV-2 in Vero cells (33). However, at each time of infection the infected cell clusters in SARS-CoV-2/1302-infected cell monolayers were smaller than those in SARS-CoV-2/0334-infected cells, consistent with the slower spread of infection for SARS-CoV-2/1302. A similar analysis of Vero E6 cells infected with SARS-CoV-2/1302 (Fig. 9A) and SARS-CoV-2/0334 (Fig. 9B), and costained with PD7 and anti-NP again showed smaller infected cell clusters at all times of infection in SARS-CoV-2/1302-infected cell monolayers. Since all antibodies showed similar clustered staining patterns, the difference in the rate of cell-to-cell spread between the two virus isolates was not antibody-specific, e.g., due to differences in RBD recognition by PD5.

Our data are consistent with localized cell-to-cell spread in the cell monolayer that correlated with high levels of cell-associated virus. However, the reason for the high level of cell-associated virus at this time of infection is currently unclear and will require further investigation. In this context, high-resolution structures of the S protein on isolated SARS-CoV-2 particles have demonstrated that low levels of the S protein trimer disassociate, leaving the S2 domain radiating from the virus envelope in an extended postfusion conformation (34). It is possible that the freely exposed fusion peptide at



the N terminus of the S2 protein may insert into the plasma membrane on infected cells and serve as an alternative transmembrane domain (35). In such a scenario, this would tether the virus particles to the surface of infected cells and facilitate the localized cell-to-cell spread of infection that we observe. The reason for the different rate of spread in the Vero cell monolayer is still uncertain. We failed to detect a significant difference in the time of appearance of the antibody-stained cells infected with either isolate in these cells. This suggests that the differences in virus spread may be due to differences between the isolates at the later stages of the virus replication; however, the mechanism behind this phenomenon will require further investigation.

**N-linked glycan maturation or furin cleavage of the S protein is not required for recognition of the RBD by PD5 in SARS-CoV-2-infected Vero E6 cells.** Furin is enriched at the Golgi complex (36), and posttranslational cleavage of the S0 protein into the S1 and S2 domains at the S1/S2 site would be expected to occur as it is trafficked through the Golgi complex. Furthermore, processing of the N-linked glycan from high-mannose cores to terminally differentiated complex glycans also occurs in the Golgi complex. The S protein contains several potential N-linked glycosylation sites, including two sites within the RBD. We therefore examined if maturation of the associated N-linked glycans and furin cleavage of the S protein was required for the recognition of the RBD by PD5.

Inhibition of the processing of S protein N-linked glycans into complex glycans was performed using the Golgi mannosidase-1 inhibitor deoxymannojirimycin (DMJ) (Fig. 10). We have previously used DMJ to examine glycan heterogeneity of the respiratory syncytial virus fusion (RSV F) protein in Vero cells (37, 38). The recombinant S protein expressed in nontreated cells and in DMJ-treated cells was examined by immunoblotting using polyS (Fig. 10Ai). A band shift in the migration of the S2 subunit (increased electrophoretic migration) in DMJ-treated cells was consistent with the presence of high-mannose cores attached to the S protein (37, 38). This was confirmed by examining the sensitivity of the recombinant S protein-associated glycans to digestion with the enzyme EndoH (Fig. 10Aii). This enzyme removes high-mannose cores from glycoproteins but is unable to remove complex N-linked glycans, and it is thus an established reagent to examine glycan maturation in glycoproteins. In nontreated cells the S protein exhibited partial sensitivity to EndoH cleavage, suggesting that individual S protein polypeptide chains contained a mixture of simple and complex glycans as described previously (39–41). In the DMJ-treated cells the S2 subunit exhibited total sensitivity to EndoH treatment as indicated by the increased migration of the S2 protein, which was consistent with the S protein in DMJ-treated Vero cells exhibiting only simple high-mannose cores. In cells expressing either the recombinant S protein (Fig. 10B) or in cells infected with SARS-CoV-2/0334 (Fig. 10C) the S protein exhibited similar polyS and PD5 staining in nontreated and DMJ-treated cells. This indicated that PD5 recognition was not dependent on the conversion of the high-mannose N-linked glycans into complex N-linked glycans, although it is acknowledged that other types of modification such as O-linked glycosylation may play a role in facilitating PD5 binding.

We have previously used the furin inhibitor decanoyl-RVKR-cmk (RVKR) to examine furin cleavage of the RSV F protein in Vero E6 cells (42). Vero E6 cells expressing the recombinant S protein were used to determine the effective concentration of decanoyl-RVKR-cmk to inhibit S protein cleavage. At 4 h posttransfection (hpt) the cells expressing the recombinant S protein were either nontreated or treated with 10, 20, or 40  $\mu\text{M}$  RVKR, and at 16 hpt the posttranslational cleavage of the S protein was examined by immunoblotting cell lysates with polyS (Fig. 11A). In nontreated cells both S0 and S2 were detected, indicating posttranslational cleavage of the S protein. Reduced levels of S2 protein were detected as the RVKR concentration was increased from 10 to 40  $\mu\text{M}$ , and at 40  $\mu\text{M}$  no residual S protein cleavage was detected. Under our experimental conditions we failed to detect any reduction in the S0 protein levels after drug treatment, which suggested that under these experimental conditions there was minimal drug toxicity, which was consistent with the lactate dehydrogenase (LDH) cytotoxicity assay which indicated 95% cell viability (R. J. Sugrue, unpublished observations).

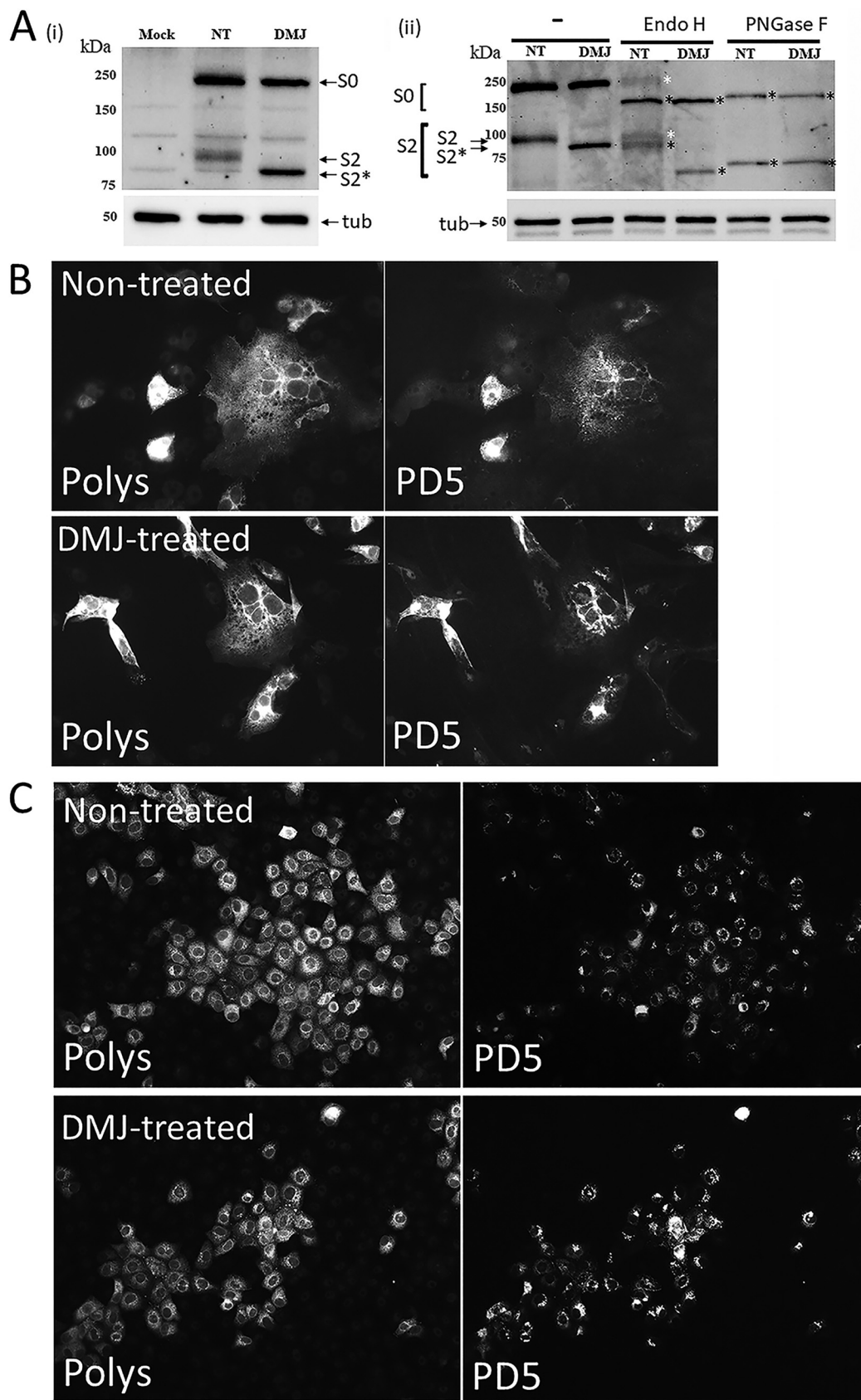


**FIG 10** Maturation of the N-linked glycans in the S protein RBD is not required for PD5 recognition. (A) (i) Cells were mock-transfected, mock and transfected with pCAGGS/S in the absence (NT) and presence of 1 mM deoxymannojirimycin (DMJ), (Continued on next page)

In a parallel analysis, nontreated and RVKR-treated cells expressing the recombinant S protein were costained with polyS and PD5 and imaged using IF microscopy (Fig. 11Bi and ii). Large antibody-costained cell clusters in nontreated cells indicated the formation of the multinucleated cell clusters, which suggested that expression of the recombinant S protein alone may be sufficient to induce membrane fusion in Vero E6 cells and is consistent with recent reports (43, 44). In A549 cells expressing the recombinant S protein we failed to detect the presence of these multinucleated cells, although PD5 and polyS staining was observed (V.Z.-Y. Lim and R. J. Sugrue, unpublished observations). The A549 cells do not express the ACE2 protein, and we presume that in Vero cells the recombinant S protein engages with the ACE2 receptor and is able to induce receptor-mediated membrane fusion. In this context the SARS-CoV-2 S protein is expected to bind to the ACE2 protein of several different animal species, including primates from which the Vero cell line is derived (45–47). Although furin cleavage of the S protein appears not to be an absolute requirement for mediating membrane fusion (43), we failed to detect the presence of multinucleated cells in the PD5 and polyS costained RVKR-treated cells. The change in staining pattern following RVKR treatment suggested a correlation between S protein cleavage and membrane fusion. However, the PD5 staining in both nontreated and RVKR-treated cells indicated that furin cleavage of the recombinant S protein was not required for RBD recognition by PD5.

The effect of RVKR treatment on PD5 recognition in Vero E6 cells infected with SARS-CoV-2/1302 (Fig. 11C) and SARS-CoV-2/0334 (Fig. 11D) was also examined. Virus-infected Vero E6 cells were either nontreated or treated with 40  $\mu$ M RVKR at 4 hpi, and at 18 hpi the cells were costained with polyS and PD5 (Fig. 11Ci and Di) and with anti-NT (Fig. 11Cii and Dii). The RVKR treatment was started at 4 h after infection to ensure no interference by the drug in establishing the initial SARS-CoV-2 infection. In the nontreated cells widespread antibody staining within the cell monolayers indicated the spread of virus infection in the cell monolayer infected with both isolates. In RVKR-treated cells the antibody staining with either isolate was restricted to individual brightly stained infected cells and smaller infected cell clusters (approximately 2 to 3 infected cells per cluster). However, RVKR treatment did not prevent PD5 recognition of the S protein and indicated that in virus-infected cells furin cleavage of the S protein was not a requirement for RBD binding by PD5. Although the S protein of SARS-CoV-2/1302 has a modified furin cleavage site, proteolytic cleavage of the S protein by furin was still required for its transmission. These data underpin the importance of the furin cleavage of the S protein in mediating virus transmission in animal models of infection (48, 49).

In a final analysis we examined if furin cleavage of the S protein was required for the recognition of the RBD by PD5 on the cell surface of Vero E6 cells infected with SARS-CoV-2/1302 (Fig. 12Ai) and SARS-CoV-2/0334 (Fig. 12Aii). While PD5 staining on nontreated cells was detected, a reduced level of PD5 surface staining on drug-treated cells infected with either virus isolate was noted. Quantification of the PD5 staining intensity on nonpermeabilized SARS-CoV-2/0334-infected cells indicated an approximately 80% reduction in PD5 staining in RVKR-treated cells (Fig. 12Aiii and iv). Individual representative nontreated and RVKR-treated nonpermeabilized and permeabilized virus-infected cells that were costained with PD5 and polyS were examined using confocal microscopy, and a series of images was

#### FIG 10 Legend (Continued)

and the cell lysates were immunoblotted with polyS. Protein species corresponding in size to the uncleaved (S0) and S2 domain of the S protein are indicated. Also indicated (S2\*) is the faster-migrating S2 domain that is formed in the presence of DMJ. (ii) Cells expressing the S protein in nontreated (NT) and DMJ-treated cells were either mock-digested (mock) or treated with EndoH and PNGase F, and the samples were immunoblotted with polyS. The migration of the EndoH-resistant (white \*) and EndoH and PNGaseF-sensitive (black\*) S protein species are indicated. In all cases immunoblotting with antitubulin (tub) is the loading control. (B) Nontreated (NT) and DMJ-treated cells expressing the recombinant S protein were costained with polyS and PD5 and imaged by immunofluorescence (IF) microscopy (objective  $\times 40$  magnification). (C) At 18 h postinfection nontreated (NT) and DMJ-treated cells infected with SARS-CoV-2/0334 were costained with polyS and PD5 and imaged by IF microscopy objective  $\times 40$  magnification.

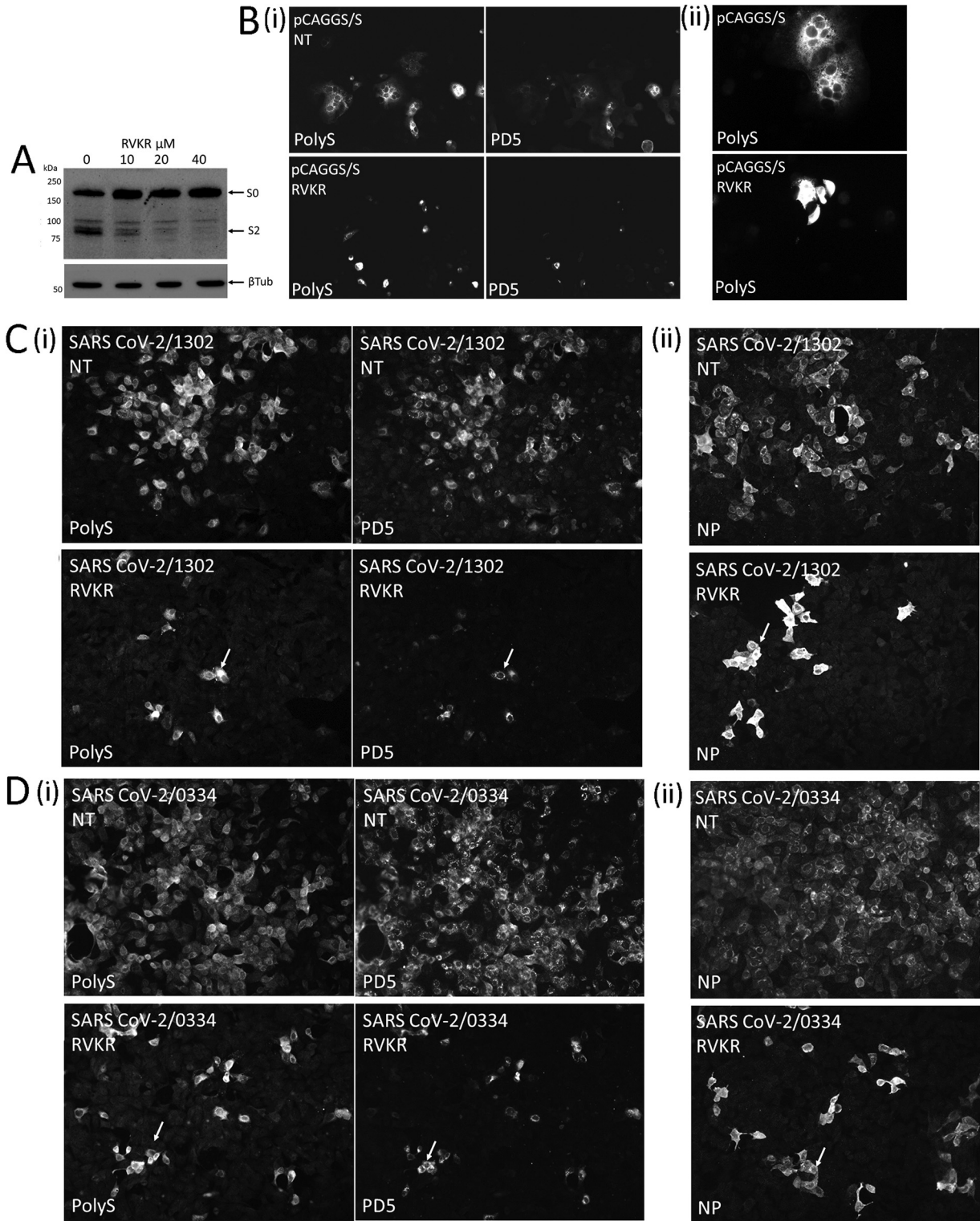


**FIG 11** Furin cleavage of the S protein is not required for recognition by PD5. (A) Vero E6 cells expressing the recombinant S protein were treated with 0, 10, 20, and 40  $\mu$ M decanoyl-RVKR-cmk (RVKR) at 4 h posttransfection (hpt), and at 16 hpt, the cell lysates were prepared and immunoblotted with polyS. The full-length S protein (S0) and S2 subunit are indicated. Tubulin ( $\beta$ Tub) is the loading control. (B) (i) Nontreated (NT) and 40  $\mu$ M RVKR-treated cells expressing the recombinant S protein were stained with PD5 and polyS and imaged using immunofluorescence (IF) microscopy (objective  $\times$ 20 magnification). (ii) Imaging of polyS-stained NT and RVKR-treated cells expressing the recombinant S protein at 16 hpt (objective  $\times$ 40 magnification). (C and D) Cells were infected with (C) SARS-CoV-2/1302 and (D) SARS-CoV-2/0334 using a multiplicity of infection of 0.01 in the absence (NT) and presence of 40  $\mu$ M RVKR. At 18 h postinfection, the cells were costained using (i) PD5 and polyS and (ii) anti-NP, and imaged using IF microscopy (objective  $\times$ 20 magnification). The reduced size of the infected cell clusters in RVKR-treated cells is highlighted (white arrows).

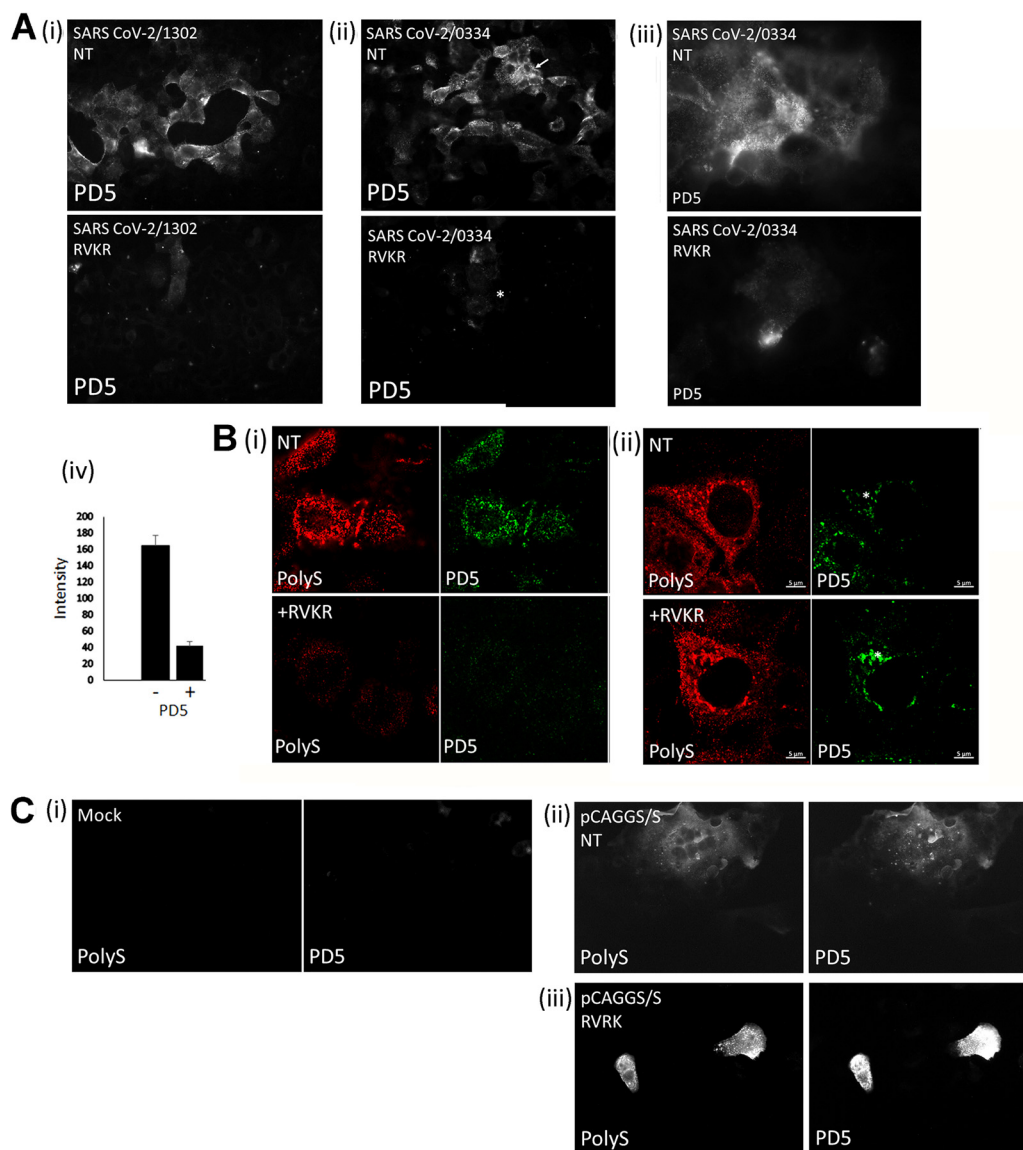


**FIG 12** Furin cleavage of the S protein is required for surface display of the PD5 epitope in virus-infected Vero E6 cells. (A) Vero E6 cells were infected with (i) SARS-CoV-2/1302 and (ii) SARS-CoV-2/0334 and either nontreated (NT) or treated with 40  $\mu$ M decanoyl-RVKR-cmk (RVKR). At 18 h postinfection (hpi), the cells were nonpermeabilized and stained with PD5 and imaged by immunofluorescence (IF) microscopy (objective  $\times$ 20 magnification). The reduced staining in RVKR-treated cells is highlighted (\*). (iii) Nontreated (NT) and RVKR-treated cells infected with SARS-CoV-2/0334 were nonpermeabilized and stained with PD5 and imaged by IF microscopy. (objective  $\times$ 100 magnification; oil immersion). (iv) The average image intensity of nontreated (-) and RVKR-treated (+) SARS-CoV-2/0334-infected cells stained with PD5 is shown.  $n = 50$  in each case. (B) The nontreated (NT) and RVKR-treated (+RVKR) SARS-CoV-2/0334-infected cells were (i) nonpermeabilized and (ii) permeabilized and were costained with PD5 and polyS. An individual image taken from a Z-stack series of images of representative cells is shown, and the individual channel images are presented. The punctate cytoplasmic PD5 staining pattern (\*) is highlighted. (C) Cells were (i) mock-transfected or transfected with pCAGGS/S and either (ii) nontreated (NT) or (iii) RVKR-treated (RVKR). The nonpermeabilized cells were costained with PD5 and polyS and imaged by IF microscopy (objective  $\times$ 40 magnification).

recorded in the Z-plane. An individual representative image slice was extracted from the image series to highlight the differences in the surface-staining intensity (Fig. 12Bi) and the cytoplasmic-staining intensity (Fig. 12Bii) under each experimental condition. This showed a similar level of cytoplasmic PD5 staining in nontreated or RVKR-treated infected cells but a reduction in the PD5 (and polyS) surface staining in RVKR-treated cells.

To determine if furin cleavage of the S protein was an essential requirement for its trafficking to the plasma membrane, nonpermeabilized mock-transfected cells (Fig. 12Ci) and cells expressing the recombinant S protein in nontreated (Fig. 12Cii) and

RVKR-treated (Fig. 12Ciii) cells were costained using polyS and PD5 and imaged using IF microscopy. Surface staining was detected on both nontreated and RVKR-treated cells using both antibodies, indicating that drug treatment did not prevent surface expression of recombinant-expressed S protein or prevent surface display of the RBD. The surface staining on nontreated cells appeared as numerous large antibody-stained clusters that were similar in appearance to the antibody-stained cell clusters detected in permeabilized cells and was consistent with S protein-mediated membrane fusion. In contrast, on RVKR-treated cells the surface staining consisted of both single-stained cells and much smaller stained cell clusters which was consistent with a reduced level of membrane fusion. The RVKR-treated cells expressing the recombinant S protein also exhibited an apparent increased surface-staining intensity when compared with that in nontreated cells. This may be due to the accumulation of the S protein in individually transfected cells in drug-treated cells compared with the more widespread S protein staining in the cell clusters in nontreated cells. Nevertheless, the recombinant S protein expression data indicated that furin cleavage of the S protein was not an inherent requirement for its trafficking to the plasma membrane.

It has been suggested that the S protein can be trafficked to the plasma membrane in virus-infected cells without being incorporated into virus particles, and that this has been proposed to induce syncytia to facilitate virus transmission. However, our data suggest that cleavage of the S protein was required for its efficient surface expression in virus-infected cells, which correlated with impaired virus cell-to-cell transmission in RVKR-treated infected cells. This may be related to other specific aspects of the virus replication cycle that restrict trafficking of the uncleaved S protein to the cell surface. For example, the S protein interacts with the M protein during virus particle formation (50), and in this context the uncleaved S protein may lead to the formation of aberrant virus particles that cannot form at the cell surface.

**Conclusion.** The PD5, PD7, and SC23 that recognize the RBD of the S protein in virus-infected cells appear to recognize only a subpopulation of the S protein that has a distinct conformation in which the RBD is accessible to antibody binding. Although much of our characterization has involved the use of PD5, the similarities in staining pattern between PD5 and the other RBD-binders suggested that PD5 was representative of these antibodies. The RBD-binders recognize the S protein at specific locations within the cell, which includes the Golgi complex and the virus particles that form at the cell surface. We failed to detect PD5 costaining with antibodies that recognize the ER compartment (R. J. Sugrue unpublished observations), indicating that RBD recognition occurs in the Golgi complex and at post-Golgi cell compartments. This further suggests that during the transit of the S protein through the Golgi complex, a conformational change in the S protein may occur that enables PD5 binding. In contrast, the recognition of the S protein by PD4 and SC29 was not dependent on RBD accessibility, and these antibodies exhibit a widespread and diffuse staining pattern in virus-infected cells. Although PD4 and SC29 do not bind to the RBD, an additional punctate staining pattern that resembles that in the RBD-binders was also apparent, suggesting that they also recognize the form of the S protein that is recognized by the RBD-binders. We do not know which domain PD4 and SC29 bind in the S protein trimer, but our data indicate that they are able to recognize multiple different forms of the S protein in a manner similar to that of the polyS antibody. There are currently several high-resolution structures that have been described that have used the soluble trimeric S protein ectodomain of both the uncleaved (S<sub>0</sub>) and the furin-cleaved (S<sub>1</sub>/S<sub>2</sub>) forms of the S protein (22, 23). In these structures it has been reported that one of the RBDs in the S protein trimer can be elevated above the S protein trimer into an open conformation and that the transformation of the RBD into the open form may be associated with increased antibody accessibility (51). These studies have suggested that the uncleaved and cleaved forms of the S protein with the RBD were preferentially in the closed and open conformation, respectively. Interestingly, structural studies of the full-length S protein trimer complex suggest that in the uncleaved S protein the RBD also exists in the closed conformation (34, 52, 53), and this is likely to better reflect the conformation of the S protein in virus-infected cells. However,

electron tomography of purified virus particles has highlighted the complexity of this issue, since these reports suggest the existence of multiple S protein conformations, including S protein trimers in a postfusion conformation consisting only of the S2 domain (34). Although our data suggest that the RBD was first detected in the Golgi complex, it is currently unclear if in the distinct S protein forms that are recognized by the PD5, PD7 and SC23 are related to the orientation of the RBD. It is possible that these antibodies recognize an alternative conformational change in the S protein during virus particle assembly that is not related to the elevation of the RBD. We can speculate that since the RBD-binders recognize conformational-specific epitopes within the RBD, these antibodies are able to detect formation of the correctly folded RBD prior to or during virus particle assembly. Future work will focus on identifying the precise binding sites of these antibodies in the S protein trimer to better understand the conformational changes in the S protein that is recognized by the RBD-binders in virus-infected cells.

**Limitations of this study.** The work described in this study primarily relies on the use of Vero E6 cells, which is an established and accepted highly permissive cell system used to propagate SARS-CoV-2. These cells lead to the production of easily definable infectious SARS-CoV-2 particles and are useful to examine the mechanics of SARS-CoV-2 infection. In this context important posttranslational modification of the S protein, such as furin cleavage and N-linked glycosylation, also occurs in these cells. However, the physiology of these nonhuman cells is likely to exhibit differences compared with the corresponding cells that are naturally infected in the airway of the human host. This may influence both the virus replication characteristics and processing of the individual virus proteins. Future work will characterize these antibodies in cells that are more representative of the human airway (e.g., nasal epithelial cells) to obtain a complete and more physiological picture of SARS-CoV-2 S protein antibody recognition.

We have used low-passaged clinical virus isolates that were isolated using tissue culture during the early stages of the pandemic in Singapore. The focus of this study was on the S protein, and in this context the S protein sequences of the individual virus isolates used in this study were genetically characterized. Although we did observe some differences in the S protein sequences that were restricted to the vicinity of the furin cleavage site, the virus isolates showed high levels of sequence identity with the corresponding S protein sequence of SARS CoV-2/WIV04, including the sequence of the RBD. Understanding the complex biology of these virus isolates was not within the scope of the current study, but the differences that we observed in the localized virus transmission of these virus isolates in tissue culture suggest subtle differences in their replication characteristics. While it is unclear how genetic variation in other virus genes would directly influence the recognition of the S protein by the antibodies used in this study, future work on the complete genetic characterization of these viruses may help to explain these differences in their biological properties that we observe.

Lastly, we have selected a panel of antibodies based in their binding properties to the S protein RBD. Although binding to the RBD was established for PD5, PD7, and SC23, we have not yet mapped their antibody binding sites on the RBD. This information should provide a much better understanding of the conformational changes in the S protein in virus-infected cells that we describe, and we will use established methodology to map their antibody binding sites on the S protein RBD in future work.

## MATERIALS AND METHODS

**Isolation of SARS-CoV-2.** Three isolates of SARS-CoV-2 viruses (designated 1302, 0563, and 0334) were isolated from nasopharyngeal samples during the early COVID-19 pandemic in Singapore. These strains were first detected using PCR primers and thermocycling conditions described in reference 54. DSO's Institutional Ethics Review Board (IRB no. 0008/2020) approval was sought before using the de-identified nasopharyngeal samples for virus isolation. The SARS-CoV-2 viruses were isolated in African green monkey kidney epithelial (Vero E6) cells (CCL-81, American Type Culture Collection, Virginia, USA) and maintained in minimum essential medium (MEM) supplemented with 10% fetal bovine serum (FBS) (Invitrogen, Carlsbad, CA, USA) and 1% penicillin and streptomycin (Invitrogen). Virus infection was carried out in the same medium with 2% FBS at 37°C in the presence of 5% CO<sub>2</sub>. The infectivity was titrated using the standard virological protocols described in reference 19. In Singapore, SARS-CoV-2 is classified as risk group 3, and this is governed by the Biological Agents and Toxins Act

(<https://www.moh.gov.sg/biosafety/about-bata>, accessed 26 November 2021). Hence, all the experiments with live SARS-CoV-2, including primary isolation were, conducted in the biosafety level 3 laboratory located at the DSO National Laboratories, with protocols (protocol no. BSL3-2020000001 and BSL3-2020000008) approved by DSO's Institutional Biosafety Committee and the Ministry of Health.

**Amplification and sequencing of the S gene.** Total nucleic acid extraction was performed on the different virus isolates and passages 1 to 3, using the QIAamp DNA minikit (Qiagen, Hilden, Germany) according to the manufacturer's instructions. For amplification of the S gene, reverse transcription was first performed on the extracted nucleic acid with a random hexamer primer using the first-strand cDNA synthesis kit (Thermo Fisher Scientific, Waltham, MA, USA) according to the manufacturer's instructions. The 3.8-kbp S gene was PCR amplified with primer SARS-CoV-2-S-F (5'-ATG TTT GTT TTT CTT GTT TTA TTG C-3') and primer SARS-CoV-2-S-R (5'-TTA TGT GTA ATG TAA TTT GAC TCC T-3') using the PCR mix consisting of 1× PCR buffer, 0.5 μM primers, 0.1 mM deoxynucleoside triphosphate (dNTP), 1.0 U Q5 high-fidelity DNA polymerase (New England Biolabs, Ipswich, MA, USA), and 5 μL of viral RNA in a final volume of 50 μL. The following thermocycling conditions were used: an initial denaturation at 98°C for 30 s, followed by 35 cycles at 98°C for 10 s, 59°C for 30 s, and 72°C for 4 min with a final extension step at 72°C for 2 min. The PCR products were electrophoresed on 1% agarose in 0.5× Tris-borate-EDTA (TBE) buffer and visualized by Midori Green (Nippon Genetics Europe GmbH, Düren, Germany) staining. The 3.8-kbp amplicons were sent for Sanger sequencing. The nucleotide or amino acid sequences were assembled and aligned with the T-Coffee program, which used both the ClustalW and Lalign methods for multiple sequence alignment (55). The full-length S gene sequences of different virus isolates and passages were next translated to amino acid sequences using the expert protein analysis system (ExpPASy) from the Swiss Bioinformatic Resource Portal (<https://www.expasy.org/>; 56). Multiple-aligned amino acid sequences of S proteins were generated using the Boxshade program of ExpPASy.

**Discovery and isolation of hMAbs.** SC23 and SC29 were generated by single B cell antibody interrogation from convalescent patient sample as described in reference 19. The human monoclonal antibodies, PD4, PD5, and PD7 were isolated from an immune phage display library constructed from the convalescent patients' B cells according to the methods described in reference 57. PD4, PD5, and PD7 were obtained by biopanning against recombinant-expressed SARS-CoV-2 S protein using the method described in reference 19.

**Antibodies and specific reagents.** The rabbit polyclonal antibody to S protein (polyS) (Sino Biological, Singapore) and anti-N (Thermo Fisher Scientific) were purchased. The anti-rabbit, anti-mouse, and anti-human IgG conjugated to Alexa 488 and Alexa 555 and the wheat germ agglutinin conjugated to Alexa 488 were purchased from Invitrogen (Thermo Fisher Scientific). The giantin rabbit polyclonal antibody was obtained from Lu Lei (Nanyang Technological University [NTU]). Publicly available sequences of the Regeneron antibodies casirivimab and imdevimab (REGN-10933 and REGN-10987, respectively) were transiently expressed in a HEK293 suspension culture and purified by protein A affinity chromatography on fast protein liquid chromatography (FPLC) as described previously (19). The furin inhibitors decanoyl-RVKR-cmk and mannosidase-1 inhibitor deoxymannojirimycin (DMJ) were purchased from Calbiochem (San Diego, CA, USA).

**Enzyme-linked immunosorbent assay (ELISA).** Recombinant spike extracellular domain (wild type [WT]) and RBD proteins were expressed and purified through a Twin-Strep tag for use in ELISA. Then, 2 μg/mL of purified protein was diluted in binding buffer (100 mM Tris-HCl, 1 mM EDTA, 150 mM NaCl, pH 8.0) and coated onto StrepTactin XT 96-well ELISA plates, 100 μL/well, for 2 h at room temperature (RT) before being washed twice with phosphate-buffered saline (PBS). Antibodies were diluted in blocking solution (2% bovine serum albumin [BSA]/PBS) to the indicated concentrations and added to the coated plate at 100 μL/well and incubated for 1 h at RT before being washed thrice with PBS/0.05% Tween. Antibody binding was detected using goat anti-human IgG Fc secondary antibody conjugated to horseradish peroxidase (Thermo Fisher Scientific), diluted 1:5,000 in blocking solution, and incubated for 1 h at RT. Plates were washed thrice with PBS/0.05% Tween and once with PBS. After washing, plates were developed with tetramethylbenzidine (TMB) substrate (Thermo Fisher Scientific). The reaction was stopped with 2 M sulfuric acid, and absorbance was measured at 450 nm.

**Neutralization assay.** The microneutralization assay was performed as described in reference 19. Briefly, antibodies at the indicated concentrations were incubated with 100 50% tissue culture infective doses (TCID<sub>50</sub>) of hCoV-19/Singapore/3/2020 virus and 2 × 10<sup>4</sup> Vero E6 cells in 100 μL of culture medium in 96-well flat-bottom plates and incubated for 72 h. The neutralization was measured using viral ToxGlo reagent (Promega, Madison, WI, USA) to determine the percentage of cell survival relative to uninfected and virus-only controls.

**Virus infection.** Vero E6 cells were seeded onto 12-mm circular glass coverslips and infected with SARS-CoV-2 at the required MOI at 37°C. When appropriate, 40 μM decanoyl-RVKR-cmk was added from 4 h postinfection. At the required time the cells were washed with PBS and fixed with 4% paraformaldehyde (Sigma-Aldrich, Burlington, MA, USA) in PBS for 30 min prior to further processing.

**Lactate dehydrogenase (LDH) cytotoxicity assay.** Cell cytotoxicity was assessed by measuring LDH release from cells using the LDH cytotoxicity assay (Promega). This was performed on nontreated and decanoyl-RVKR-cmk-treated Vero cells following the manufacturer's instructions.

**Recombinant S protein expression.** The S gene of SARS-CoV-2 (accession no. [MN908947](https://www.ncbi.nlm.nih.gov/nuclseq/NC_022922.3)) was synthesized by Twist BioSciences (San Francisco, CA, USA). The codon-optimized full-length S gene (nucleotide residues 1 to 1273) was assembled as previously described (19) and cloned into the recombinant pCAGGS vector to create pCAGGS/S. For S1 subunit and RBD expression, only residues 1 to 685 (S1) and 331 to 524 (RBD) were cloned together with a c-flag and a c-myc tag, respectively. The fragments were cloned into pCAGGS to generate pCAGGS/S1 and pCAGGS/RBD. Bulk preparation of all plasmids was performed using the plasmid Midiprep kit (Qiagen). Cells (1 × 10<sup>5</sup>) were transfected into HEK293 with



1  $\mu$ g plasmid DNA using Lipofectamine 2000 (Invitrogen) following the manufacturer's instructions. The transfected cells were maintained at 37°C until the time of sample processing.

**Immunofluorescence microscopy.** The cells on 12-mm circular glass coverslips were fixed with 4% paraformaldehyde (Sigma-Aldrich) and washed with PBS. The cells were either nonpermeabilized or permeabilized using 0.1% Triton X-100 in PBS at 4°C for 15 min prior to antibody staining. The cells were stained with the appropriate primary and secondary antibody combinations and mounted on microscope slides using CitiFluor. The stained cells were imaged using a Nikon Eclipse 80i Microscope (Nikon Corporation, Tokyo, Japan) with an Etiga 2000R camera (Q Imaging, Teledyne Photometrics, Tucson AZ, USA) attached. The images of immunofluorescence-stained cells were recorded using Q Capture Pro ver. 5.0.1.26 (Q Imaging, Teledyne Photometrics). Imaging for confocal microscopy was performed with a 710 confocal microscope (Zeiss, Oberkochen, Germany) with Airyscan using the appropriate machine settings. The recorded images were examined and processed using Zen ver. 2.3 software (Zeiss).

**Scanning electron microscopy (SEM).** The cells on the 13-mm glass coverslips were fixed using 4% paraformaldehyde (Sigma-Aldrich) in PBS and washed with PBS. The cells were then fixed sequentially using 3% glutaraldehyde (Sigma-Aldrich) and 1% osmium tetroxide (Sigma-Aldrich) and dehydrated using an ethanol gradient, and critical point drying was performed as described previously (58). The processed cells were gold-coated and mounted on aluminum stubs and imaged with a Quanta 650 FEG scanning electron microscope (FEI Company, Oregon, USA) using the appropriate machine settings.

## SUPPLEMENTAL MATERIAL

Supplemental material is available online only.

**SUPPLEMENTAL MATERIAL**, PDF file, 0.1 MB.

## ACKNOWLEDGMENTS

The work was supported by DSO National Laboratories and Nanyang Technological University.

We acknowledge Sok-Kiang Lau, Jin-Phang Loh, Wee-Hong Koh, Hwee-Teng Low, Jasper Chin-Wen Liaw, Janet Seok-Wei Chew, Xiao-Fang Lim, Elizabeth Ai-Sim Lim, Tan Jie Ling, and Sian-Foong Ling for technical assistance and the diagnostics performed on the samples and the facility team (Loh Siang Gary, Mok-Wei Heng, Chang-Lin Chang, and Lay-Tin Aw) for their assistance.

We declare no conflict of interest.

Conceptualization, R.J.S., C.E.-Z.C., B.-H.T.; methodology, A.P.-C.L., S.L.-K.S., D.-H.C., S.K.-K.W., C.-G.N., J.-H.L., V.Z.-Y.L., P.-S.W., K.-M.L., S.-K.L., Y.-C.L.; data analysis, C.E.-Z.C., C.-G.N., B.-H.T., R.J.S.; data curation, B.-H.T., R.J.S.; writing, reviewing, and editing, B.-H.T., R.J.S.; project administration, B.-H.T., C.E.-Z.C.

## REFERENCES

- Li Q, Guan X, Wu P, Wang X, Zhou L, Tong Y, Ren R, Leung KSM, Lau EHY, Wong JY, Xing X, Xiang N, Wu Y, Li C, Chen Q, Li D, Liu T, Zhao J, Liu M, Tu W, Chen C, Jin L, Yang R, Wang Q, Zhou S, Wang R, Liu H, Luo Y, Liu Y, Shao G, Li H, Tao Z, Yang Y, Deng Z, Liu B, Ma Z, Zhang Y, Shi G, Lam TTY, Wu JT, Gao GF, Cowling BJ, Yang B, Leung GM, Feng Z. 2020. Early transmission dynamics in Wuhan, China, of novel coronavirus-infected pneumonia. *N Engl J Med* 382:1199–1207. <https://doi.org/10.1056/NEJMoa2001316>.
- Zhu N, Zhang D, Wang W, Li X, Yang B, Song J, Zhao X, Huang B, Shi W, Lu R, Niu P, Zhan F, Ma X, Wang D, Xu W, Wu G, Gao GF, Tan W, China Novel Coronavirus Investigating and Research Team. 2020. A novel coronavirus from patients with pneumonia in China, 2019. *N Engl J Med* 382:727–733. <https://doi.org/10.1056/NEJMoa2001017>.
- van der Hoek L. 2007. Human coronaviruses: what do they cause? *Antivir Ther* 12:651–658. <https://doi.org/10.1177/135965350701200501.1>.
- Drosten C, Günther S, Preiser W, van der Werf S, Brodt H-R, Becker S, Rabenau H, Panning M, Kolesnikova L, Fouchier RAM, Berger A, Burguière A-M, Cinatl J, Eickmann M, Escriou N, Grywna K, Kramme S, Manuguerra J-C, Müller S, Rickerts V, Stürmer M, Vieth S, Klenk H-D, Osterhaus ADME, Schmitz H, Doerr HW. 2003. Identification of a novel coronavirus in patients with severe acute respiratory syndrome. *N Engl J Med* 348:1967–1976. <https://doi.org/10.1056/NEJMoa030747>.
- Nickbakhsh S, Ho A, Marques DFP, McMenamin J, Gunson RN, Murcia PR. 2020. Epidemiology of seasonal coronaviruses: establishing the context for the emergence of coronavirus disease 2019. *J Infect Dis* 222:17–25. <https://doi.org/10.1093/infdis/jiaa185>.
- Fehr AR, Perlman S. 2015. Coronaviruses: an overview of their replication and pathogenesis. *Methods Mol Biol* 1282:1–23. [https://doi.org/10.1007/978-1-4939-2438-7\\_1](https://doi.org/10.1007/978-1-4939-2438-7_1).
- Zhou P, Yang X-L, Wang X-G, Hu B, Zhang L, Zhang W, Si H-R, Zhu Y, Li B, Huang C-L, Chen H-D, Chen J, Luo Y, Guo H, Jiang R-D, Liu M-Q, Chen Y, Shen X-R, Wang X, Zheng X-S, Zhao K, Chen Q-J, Deng F, Liu L-L, Yan B, Zhan F-X, Wang Y-Y, Xiao G-F, Shi Z-L. 2020. A pneumonia outbreak associated with a new coronavirus of probable bat origin. *Nature* 579:270–273. <https://doi.org/10.1038/s41586-020-2012-7>.
- Veneti L, Seppälä E, Larsdatter Storm M, Valcarcel Salamanca B, Alnes Buenes E, Aasand N, Naseer U, Bragstad K, Hungnes O, Bøås H, Kvåle R, Golestani K, Feruglio S, Vold L, Nygård K, Whittaker R. 2021. Increased risk of hospitalisation and intensive care admission associated with reported cases of SARS-CoV-2 variants B.1.1.7 and B.1.351 in Norway, December 2020 -May 2021. *PLoS One* 16:e0258513. <https://doi.org/10.1371/journal.pone.0258513>.
- Bager P, Wohlfahrt J, Fonager J, Rasmussen M, Albertsen M, Michaelsen TY, Møller CH, Ethelberg S, Legarth R, Button MSF, Gubbels S, Voldstedlund M, Mølbak K, Skov RL, Fomsgaard A, Krause TG. 2021. Risk of hospitalisation associated with infection with SARS-CoV-2 lineage B.1.1.7 in Denmark: an observational cohort study. *Lancet Infect Dis* 21:1507–1517. [https://doi.org/10.1016/S1473-3099\(21\)00290-5](https://doi.org/10.1016/S1473-3099(21)00290-5).
- Challen R, Brooks-Pollock E, Read JM, Dyson L, Tsaneva-Atanasova K, Danon L. 2021. Risk of mortality in patients infected with SARS-CoV-2 variant of concern 202012/1: matched cohort study. *BMJ* 372:n579. <https://doi.org/10.1136/bmj.n579>.

11. Hu B, Guo H, Zhou P, Shi Z-L. 2021. Characteristics of SARS-CoV-2 and COVID-19. *Nat Rev Microbiol* 19:141–154. <https://doi.org/10.1038/s41579-020-00459-7>.
12. Tang T, Jaimes JA, Bidon MK, Straus MR, Daniel S, Whittaker GR. 2021. Proteolytic activation of SARS-CoV-2 spike at the S1/S2 boundary: potential role of proteases beyond furin. *ACS Infect Dis* 7:264–272. <https://doi.org/10.1021/acscinfeddis.0c00701>.
13. Bertram S, Glowacka I, Blazejewski P, Soilleux E, Allen P, Danisch S, Steffen I, Choi S-Y, Park Y, Schneider H, Schughart K, Pöhlmann S. 2010. TMPRSS2 and TMPRSS4 facilitate trypsin-independent spread of influenza virus in Caco-2 cells. *J Virol* 84:10016–10025. <https://doi.org/10.1128/JVI.00239-10>.
14. Simmons G, Gosalia DN, Rennekamp AJ, Reeves JD, Diamond SL, Bates P. 2005. Inhibitors of cathepsin L prevent severe acute respiratory syndrome coronavirus entry. *Proc Natl Acad Sci U S A* 102:11876–11881. <https://doi.org/10.1073/pnas.0505577102>.
15. Kabir MA, Ahmed R, Chowdhury R, Iqbal SMA, Paulmurugan R, Demirci U, Asghar W. 2021. Management of COVID-19: current status and future prospects. *Microbes Infect* 23:104832. <https://doi.org/10.1016/j.micinf.2021.104832>.
16. Brouwer PJM, Caniels TG, van der Straten K, Nitselaar JL, Aldon Y, Bangaru S, Torres JL, Okba NMA, Claireaux M, Kerster G, Bentlage AEH, van Haaren MM, Guerra D, Burger JA, Schermer EE, Verheul KD, van der Velde N, van der Kooi A, van Schooten J, van Breemen MJ, Bijl TPL, Sliepen K, Aartse A, Derking R, Bontjer I, Kootstra NA, Wiersinga WJ, Vidarsson G, Haagmans BL, Ward AB, de Bree GJ, Sanders RW, van Gils MJ. 2020. Potent neutralizing antibodies from COVID-19 patients define multiple targets of vulnerability. *Science* 369:643–650. <https://doi.org/10.1126/science.abc5902>.
17. Jennewein MF, MacCamy AJ, Akins NR, Feng J, Homad LJ, Hurlburt NK, Seydoux E, Wan Y-H, Stuart AB, Edara VV, Floyd K, Vanderheiden A, Mascola JR, Doria-Rose N, Wang L, Yang ES, Chu HY, Torres JL, Ozorowski G, Ozorowski AB, Whaley RE, Cohen KW, Pancera M, McElrath MJ, Englund JA, Finzi A, Suthar MS, McGuire AT, Stamatatos L. 2021. Isolation and characterization of cross-neutralizing coronavirus antibodies from COVID-19+ subjects. *bioRxiv* <https://doi.org/10.1101/2021.03.23.436684>.
18. Zost SJ, Gilchuk P, Case JB, Binshtein E, Chen RE, Nkolola JP, Schäfer A, Reidy JX, Trivette A, Nargi RS, Sutton RE, Suryadevara N, Martinez DR, Williamson LE, Chen EC, Jones T, Day S, Myers L, Hassan AO, Kafai NM, Winkler ES, Fox JM, Shrihari S, Mueller BK, Meiler J, Chandrashekar A, Mercado NB, Steinhardt JJ, Ren K, Loo Y-M, Kallewaard NL, McCune BT, Keeler SP, Holtzman MJ, Barouch DH, Galinski LE, Baric RS, Thackray LB, Diamond MS, Carnahan RH, Crowe JE, Jr. 2020. Potently neutralizing and protective human antibodies against SARS-CoV-2. *Nature* 584:443–449. <https://doi.org/10.1038/s41586-020-2548-6>.
19. Chan CEZ, Seah SGK, Chye DH, Massey S, Torres M, Lim APC, Wong SKK, Neo JYJ, Wong PS, Lim JH, Loh GSL, Wang D, Boyd-Kirkup JD, Guan S, Thakkar D, Teo GH, Purushothaman K, Hutchinson PE, Young BE, Low JG, MacAry PA, Hentze H, Prativadibhayankara VS, Ethirajulu K, Comer JE, Tseng C-TK, Barrett ADT, Ingram PJ, Brasel T, Hanson BJ. 2021. The Fc-mediated effector functions of a potent SARS-CoV-2 neutralizing antibody, SC31, isolated from an early convalescent COVID-19 patient, are essential for the optimal therapeutic efficacy of the antibody. *PLoS One* 16:e0253487. <https://doi.org/10.1371/journal.pone.0253487>.
20. Baum A, Ajithdoss D, Copin R, Zhou A, Lanza K, Negron N, Ni M, Wei Y, Mohammadi K, Musser B, Atwal GS, Oyejide A, Goez-Gazi Y, Dutton J, Clemmons E, Staples HM, Bartley C, Klaffke B, Alfson K, Gazi M, Gonzalez O, Dick E, Carrion R, Pessaint L, Porto M, Cook A, Brown R, Ali V, Greenhouse J, Taylor T, Andersen H, Lewis MG, Stahl N, Murphy AJ, Yancopoulos GD, Kyrtatsos CA. 2020. REGN-COV2 antibodies prevent and treat SARS-CoV-2 infection in rhesus macaques and hamsters. *Science* 370:1110–1115. <https://doi.org/10.1126/science.abe2402>.
21. Weinreich DM, Sivapalasingam S, Norton T, Ali S, Gao H, Bhore R, Musser BJ, Soo Y, Rofail D, Im J, Perry C, Pan C, Hosain R, Mahmood A, Davis JD, Turner KC, Hooper AT, Hamilton JD, Baum A, Kyrtatsos CA, Kim Y, Cook A, Kampman W, Kohli A, Sachdeva Y, Graber X, Kowal B, DiCioccio T, Stahl N, Lipsich L, Braunstein N, Herman G, Yancopoulos GD, Trial Investigators. 2021. REGN-COV2, a neutralizing antibody cocktail, in outpatients with Covid-19. *N Engl J Med* 384:238–251. <https://doi.org/10.1056/NEJMoa2035002>.
22. Wrobel AG, Benton DJ, Xu P, Roustan C, Martin SR, Rosenthal PB, Skehel JJ, Gamblin SJ. 2020. SARS-CoV-2 and bat RaTG13 spike glycoprotein structures inform on virus evolution and furin-cleavage effects. *Nat Struct Mol Biol* 27:763–767. <https://doi.org/10.1038/s41594-020-0468-7>.
23. Wrapp D, Wang N, Corbett KS, Goldsmith JA, Hsieh C-L, Abiona O, Graham BS, McLellan JS. 2020. Cryo-EM structure of the 2019-nCoV spike in the prefusion conformation. *Science* 367:1260–1263. <https://doi.org/10.1126/science.abb2507>.
24. Andrés C, García-Cehic D, Gregori J, Piñana M, Rodríguez-Frias F, Guerrero-Murillo M, Esperalba J, Rando A, Gotteris L, Codina MG, Quer S, Martín MC, Campins M, Ferrer R, Almirante B, Esteban JI, Pumarola T, Antón A, Quer J. 2020. Naturally occurring SARS-CoV-2 gene deletions close to the spike S1/S2 cleavage site in the viral quasispecies of COVID19 patients. *Emerg Microbes Infect* 9:1900–1911. <https://doi.org/10.1080/22221751.2020.1806735>.
25. Lontok E, Corse E, Machamer CE. 2004. Intracellular targeting signals contribute to localization of coronavirus spike proteins near the virus assembly site. *J Virol* 78:5913–5922. <https://doi.org/10.1128/JVI.78.11.5913-5922.2004>.
26. Copin R, Baum A, Wloga E, Pascal KE, Giordano S, Fulton BO, Zhou A, Negron N, Lanza K, Chan N, Coppola A, Chiu J, Ni M, Wei Y, Atwal GS, Hernandez AR, Saotome K, Zhou Y, Franklin MC, Hooper AT, McCarthy S, Hamon S, Hamilton JD, Staples HM, Alfson K, Carrion R, Ali S, Norton T, Somersan-Karakaya S, Sivapalasingam S, Herman GA, Weinreich DM, Lipsich L, Stahl N, Murphy AJ, Yancopoulos GD, Kyrtatsos CA. 2021. The monoclonal antibody combination REGEN-COV protects against SARS-CoV-2 mutational escape in preclinical and human studies. *Cell* 184:3949–3961.e11. <https://doi.org/10.1016/j.cell.2021.06.002>.
27. Starr TN, Greaney AJ, Addetia A, Hannon WW, Choudhary MC, Dingens AS, Li JZ, Bloom JD. 2021. Prospective mapping of viral mutations that escape antibodies used to treat COVID-19. *Science* 371:850–854. <https://doi.org/10.1126/science.abc9302>.
28. Zhao P, Praisman JL, Grant OC, Cai Y, Xiao T, Rosenbalm KE, Aoki K, Kellman BP, Bridger R, Barouch DH, Brindley MA, Lewis NE, Tiemeyer M, Chen B, Woods RJ, Wells L. 2020. Virus-receptor interactions of glycosylated SARS-CoV-2 spike and human ACE2 receptor. *Cell Host Microbe* 28:586–601.e6. <https://doi.org/10.1016/j.chom.2020.08.004>.
29. Laue M, Kauter A, Hoffmann T, Möller L, Michel J, Nitsche A. 2021. Morphometry of SARS-CoV and SARS-CoV-2 particles in ultrathin plastic sections of infected Vero cell cultures. *Sci Rep* 11:3515. <https://doi.org/10.1038/s41598-021-82852-7>.
30. Zeng C, Evans JP, King T, Zheng Y-M, Oltz EM, Whelan SPJ, Saif L, Peeples ME, Liu S-L. 2021. SARS-CoV-2 spreads through cell-to-cell transmission. *bioRxiv* <https://doi.org/10.1101/2021.06.01.446579>.
31. Caldas LA, Carneiro FA, Higa LM, Monteiro FL, da Silva GP, da Costa LJ, Durigon EL, Tanuri A, de Souza W. 2020. Ultrastructural analysis of SARS-CoV-2 interactions with the host cell via high resolution scanning electron microscopy. *Sci Rep* 10:16099. <https://doi.org/10.1038/s41598-020-73162-5>.
32. Hirano N, Fujiwara K, Matumoto M. 1976. Mouse hepatitis virus (MHV-2). Plaque assay and propagation in mouse cell line DBT cells. *Jpn J Microbiol* 20:219–225. <https://doi.org/10.1111/j.1348-0421.1976.tb00978.x>.
33. Harcourt J, Tamin A, Lu X, Kamili S, Sakthivel SK, Murray J, Queen K, Tao Y, Paudyal CR, Zhang J, Li Y, Uehara A, Wang H, Goldsmith C, Bullock HA, Wang L, Whitaker B, Lynch B, Gautam R, Schindewolf C, Lokugamage KG, Scharton D, Plante JA, Mirchandani D, Widen SG, Narayanan K, Makino S, Ksiazek TG, Plante KS, Weaver SC, Lindstrom S, Tong S, Menachery VD, Thornburg NG. 2020. Isolation and characterization of SARS-CoV-2 from the first US COVID-19 patient. *bioRxiv* <https://doi.org/10.1101/2020.03.02.972935>.
34. Cai Y, Zhang J, Xiao T, Peng H, Sterling SM, Walsh RM, Rawson S, Rits-Volloch S, Chen B. 2020. Distinct conformational states of SARS-CoV-2 spike protein. *Science* 369:1586–1592. <https://doi.org/10.1126/science.abd4251>.
35. Lozada C, Barlow TMA, Gonzalez S, Lubin-Germain N, Ballet S. 2021. Identification and characteristics of fusion peptides derived from enveloped viruses. *Front Chem* 9:689006. <https://doi.org/10.3389/fchem.2021.689006>.
36. Molloy SS, Thomas L, VanSlyke JK, Stenberg PE, Thomas G. 1994. Intracellular trafficking and activation of the furin proprotein convertase: localization to the TGN and recycling from the cell surface. *EMBO J* 13:18–33. <https://doi.org/10.1002/j.1460-2075.1994.tb06231.x>.
37. McDonald TP, Jeffrey CE, Li P, Rixon HWM, Brown G, Aitken JD, MacLellan K, Sugrue RJ. 2006. Evidence that maturation of the N-linked glycans of the respiratory syncytial virus (RSV) glycoproteins is required for virus-mediated cell fusion: The effect of alpha-mannosidase inhibitors on RSV infectivity. *Virology* 350:289–301. <https://doi.org/10.1016/j.virol.2006.01.023>.
38. McDonald TP, Sugrue RJ. 2007. The use of two-dimensional SDS-PAGE to analyze the glycan heterogeneity of the respiratory syncytial virus fusion protein. *Methods Mol Biol* 379:97–108. [https://doi.org/10.1007/978-1-59745-393-6\\_7](https://doi.org/10.1007/978-1-59745-393-6_7).
39. Miller LM, Barnes LF, Raab SA, Draper BE, El-Baba TJ, Lutomski CA, Robinson CV, Clemmer DE, Jarrold MF. 2021. Heterogeneity of glycan processing on trimeric SARS-CoV-2 spike protein revealed by charge detection mass spectrometry. *J Am Chem Soc* 143:3959–3966. <https://doi.org/10.1021/jacs.1c00353>.

40. Watanabe Y, Allen JD, Wrapp D, McLellan JS, Crispin M. 2020. Site-specific glycan analysis of the SARS-CoV-2 spike. *Science* 369:330–333. <https://doi.org/10.1126/science.abb9983>.
41. Yao H, Song Y, Chen Y, Wu N, Xu J, Sun C, Zhang J, Weng T, Zhang Z, Wu Z, Cheng L, Shi D, Lu X, Lei J, Crispin M, Shi Y, Li L, Li S. 2020. Molecular architecture of the SARS-CoV-2 virus. *Cell* 183:730–738.e13. <https://doi.org/10.1016/j.cell.2020.09.018>.
42. Sugrue RJ, Brown C, Brown G, Aitken J, Rixon HWM. 2001. Furin cleavage of the respiratory syncytial virus fusion protein is not a requirement for its transport to the surface of virus-infected cells. *J Gen Virol* 82:1375–1386. <https://doi.org/10.1099/0022-1317-82-6-1375>.
43. Papa G, Mallery DL, Albecka A, Welch LG, Cattin-Ortolá J, Luptak J, Paul D, McMahon HT, Goodfellow IG, Carter A, Munro S, James LC. 2021. Furin cleavage of SARS-CoV-2 Spike promotes but is not essential for infection and cell-cell fusion. *PLoS Pathog* 17:e1009246. <https://doi.org/10.1371/journal.ppat.1009246>.
44. Xia S, Lan Q, Su S, Wang X, Xu W, Liu Z, Zhu Y, Wang Q, Lu L, Jiang S. 2020. The role of furin cleavage site in SARS-CoV-2 spike protein-mediated membrane fusion in the presence or absence of trypsin. *Signal Transduct Target Ther* 5:92. <https://doi.org/10.1038/s41392-020-0184-0>.
45. Gao S, Luan J, Cui H, Zhang L. 2021. ACE2 isoform diversity predicts the host susceptibility of SARS-CoV-2. *Transbound Emerg Dis* 68:1026–1032. <https://doi.org/10.1111/tbed.13773>.
46. Conceicao C, Thakur N, Human S, Kelly JT, Logan L, Bialy D, Bhat S, Stevenson-Leggett P, Zagrajek AK, Hollinghurst P, Varga M, Tsigirigoti C, Tully M, Chiu C, Moffat K, Silesian AP, Hammond JA, Maier HJ, Bickerton E, Shelton H, Dietrich I, Graham SC, Bailey D. 2020. The SARS-CoV-2 Spike protein has a broad tropism for mammalian ACE2 proteins. *PLoS Biol* 18:e3001016. <https://doi.org/10.1371/journal.pbio.3001016>.
47. Damas J, Hughes GM, Keough KC, Painter CA, Persky NS, Corbo M, Hiller M, Koepfli K-P, Pfenning AR, Zhao H, Genereux DP, Swofford R, Pollard KS, Ryder OA, Nweeia MT, Lindblad-Toh K, Teeling EC, Karlsson EK, Lewin HA. 2020. Broad host range of SARS-CoV-2 predicted by comparative and structural analysis of ACE2 in vertebrates. *Proc Natl Acad Sci U S A* 117:22311–22322. <https://doi.org/10.1073/pnas.2010146117>.
48. Peacock TP, Goldhill DH, Zhou J, Baillon L, Frise R, Swann OC, Kugathasan R, Penn R, Brown JC, Sanchez-David RY, Braga L, Williamson MK, Hassard JA, Staller E, Hanley B, Osborn M, Giacca M, Davidson AD, Matthews DA, Barclay WS. 2021. The furin cleavage site in the SARS-CoV-2 spike protein is required for transmission in ferrets. *Nat Microbiol* 6:899–909. <https://doi.org/10.1038/s41564-021-00908-w>.
49. Johnson BA, Xie X, Bailey AL, Kalveram B, Lokugamage KG, Muruato A, Zou J, Zhang X, Juelich T, Smith JK, Zhang L, Bopp N, Schindewolf C, Vu M, Vanderheiden A, Winkler ES, Swetnam D, Plante JA, Aguilar P, Plante KS, Popov V, Lee B, Weaver SC, Suthar MS, Routh AL, Ren P, Ku Z, An Z, Debbink K, Diamond MS, Shi P-Y, Freiberg AN, Menachery VD. 2021. Loss of furin cleavage site attenuates SARS-CoV-2 pathogenesis. *Nature* 591:293–299. <https://doi.org/10.1038/s41586-021-03237-4>.
50. Duan L, Zheng Q, Zhang H, Niu Y, Lou Y, Wang H. 2020. The SARS-CoV-2 spike glycoprotein biosynthesis, structure, function, and antigenicity: implications for the design of spike-based vaccine immunogens. *Front Immunol* 11:576622. <https://doi.org/10.3389/fimmu.2020.576622>.
51. Harvey WT, Carabelli AM, Jackson B, Gupta RK, Thomson EC, Harrison EM, Ludden C, Reeve R, Rambaut A, Peacock SJ, Robertson DL, COVID-19 Genomics UK (COG-UK) Consortium. 2021. SARS-CoV-2 variants, spike mutations and immune escape. *Nat Rev Microbiol* 19:409–424. <https://doi.org/10.1038/s41579-021-00573-0>.
52. Bangaru S, Ozorowski G, Turner HL, Antanasijevic A, Huang D, Wang X, Torres JL, Diedrich JK, Tian J-H, Portnoff AD, Patel N, Massare MJ, Yates JR, Nemazee D, Paulson JC, Glenn G, Smith G, Ward AB. 2020. Structural analysis of full-length SARS-CoV-2 spike protein from an advanced vaccine candidate. *Science* 370:1089–1094. <https://doi.org/10.1126/science.abe1502>.
53. Turoňová B, Sikora M, Schürmann C, Hagen WJH, Welsch S, Blanc FEC, von Bülow S, Gecht M, Bagola K, Hörner C, van Zandbergen G, Landry J, de Azevedo NTD, Mosalaganti S, Schwarz A, Covino R, Mühlebach MD, Hummer G, Krijnse Locker J, Beck M. 2020. In situ structural analysis of SARS-CoV-2 spike reveals flexibility mediated by three hinges. *Science* 370:203–208. <https://doi.org/10.1126/science.abd5223>.
54. Chia PY, Coleman KK, Tan YK, Ong SWX, Gum M, Lau SK, Lim XF, Lim AS, Sutjipto S, Lee PH, Son TT, Young BE, Milton DK, Gray GC, Schuster S, Barkham T, De PP, Vasoo S, Chan M, Ang BSP, Tan BH, Leo Y-S, Ng O-T, Wong MSY, Marimuthu K, Singapore 2019 Novel Coronavirus Outbreak Research Team. 2020. Detection of air and surface contamination by SARS-CoV-2 in hospital rooms of infected patients. *Nat Commun* 11:2800. <https://doi.org/10.1038/s41467-020-16670-2>.
55. Notredame C, Higgins DG, Heringa J. 2000. T-Coffee: a novel method for fast and accurate multiple sequence alignment. *J Mol Biol* 302:205–217. <https://doi.org/10.1006/jmbi.2000.4042>.
56. Gasteiger E, Gattiker A, Hoogland C, Ivanyi I, Appel RD, Bairoch A. 2003. ExPASy: the proteomics server for in-depth protein knowledge and analysis. *Nucleic Acids Res* 31:3784–3788. <https://doi.org/10.1093/nar/gkg563>.
57. de Haard HJ, van Neer N, Reurs A, Hufton SE, Roovers RC, Henderikx P, de Bruïne AP, Arends JW, Hoogenboom HR. 1999. A large non-immunized human Fab fragment phage library that permits rapid isolation and kinetic analysis of high affinity antibodies. *J Biol Chem* 274:18218–18230. <https://doi.org/10.1074/jbc.274.26.18218>.
58. Jeffree CE, Rixon HWM, Brown G, Aitken J, Sugrue RJ. 2003. Distribution of the attachment (G) glycoprotein and GM1 within the envelope of mature respiratory syncytial virus filaments revealed using field emission scanning electron microscopy. *Virology* 306:254–267. [https://doi.org/10.1016/S0042-6822\(02\)00016-8](https://doi.org/10.1016/S0042-6822(02)00016-8).